Science
AAAS

Supplementary Materials for

Imprinting the quantum statistics of photons on free electrons

Raphael Dahan *et al.*

Corresponding author: Ido Kaminer, kaminer@technion.ac.il

Science **373**, eabj7128 (2021)
DOI: 10.1126/science.abj7128

The PDF file includes:

Materials and Methods

The experimental setup

The experimental apparatus is described in the subsections below: the electron microscope, the light system (laser and amplifier), the fabrication, and inverse design of our silicon-photonic nanostructure.

The electron microscope and light source

The experiments were performed using a system based on a JEOL JEM-2100 Plus TEM equipped with a Gatan GIF system and operating using a LaB_6 electron filament in thermal emission mode. The TEM was modified to enable coupling light into the sample (described schematically in Fig. 3 from the main text), used previously for ultrafast TEM experiments (*38, 40*).

Data acquisition is done in the converged beam electron diffraction (CBED) mode. The electron beam diameter in the focal plane was 30 nm with a convergence angle of 0.3 mrad and a 0.6 eV FWHM zero-loss energy width. We aligned the nanostructure channel to the electron trajectory using a double-tilt holder (Mel-Build Hata Holder) with a custom cartridge to avoid shadowing the optical beam.

A CW-driven distributed feedback (DFB) laser (QLD106p-64D0) emitting at 1060 nm served as a seed for a two-stage Yb fiber amplifier with a 4 nm filter between the two stages. The laser spot size was focused with a cylindrical lens to 51 μm FWHM along the electron trajectory and 8.5 μm FWHM in the direction perpendicular to the electron and to the nanostructure channel.

Fabrication of the silicon-photonic nanostructure

The silicon-photonic nanostructure was fabricated by electron beam lithography (100 keV) and cryogenic reactive-ion etching of 1-5 Ωcm phosphorus-doped silicon to a depth of 2.8±0.1 μm (*87*). The surrounding substrate was etched away to form a 30-μm-high mesa, providing clearance for both electron beam and light beam.

Photonic inverse design of the silicon-photonic nanostructure

We used an open-source Python package based on a 2D-FDFD simulation (*42*). The structure was optimized over a 5-μm-wide design region in the xz-plane, containing a 250-nm-wide vacuum channel in the center for the electrons to propagate through. Periodic boundaries were applied along the z-direction, enforcing the periodicity of 733 nm, and perfectly matched layers were defined along x. A transverse-magnetic plane wave was excited from one side, and the resulting electric field E_z was computed in the center of the channel to find the acceleration gradient, which served as the objective function of the optimization (*11, 88*). The silicon-photonic nanostructure is shown in Fig. S1.

Supplementary Text

S1. The theory of quantum and random walk

In this section, we consider the interaction between light and free electrons and show how it can be described in terms of quantum walk, random walk, and the combination of the two.

S1.1. The connection between the interaction of a free electron with coherent-state light to the quantum walk model

Let us consider the following model describing the interaction between light and an electron in a discrete energy ladder. The energy ladder forms a synthetic dimension in which the electron makes discrete steps. At each step, the electron has the following three options: (i) absorb a photon and climb up one step in the energy ladder; (ii) emit a photon and go down one step in the energy ladder; (iii) no interaction, retaining its previous energy. Moreover, in this simple model, we consider that the emission and absorption have the same probabilities (which is a good approximation for large photon numbers). We further assume that the light is unperturbed by the interaction so we can consider the probabilities as constants throughout the walk. The electron wavefunction can be written as a column vector of complex number amplitudes, where each component of the column represents a monoenergetic state:

$$|\psi\rangle = (\dots, \psi_{-1}, \psi_0, \psi_1, \dots)^T, \tag{S1.1}$$

which denotes $|\psi\rangle \equiv \sum_k \psi_k |E_0 + k\hbar\omega\rangle$, where $|E_0 + k\hbar\omega\rangle$ is a monoenergetic state with the energy $E_0 + k\hbar\omega$ (E_0 is the initial energy). After $n+1$ steps, the k^{th} component has the following form:

$$\psi_k^{(n+1)} = \sqrt{1 - 2|c|^2}\psi_k^{(n)} + c\psi_{k+1}^{(n)} + c^*\psi_{k-1}^{(n)}, \tag{S1.2}$$

where c is a complex number describing the transition amplitude of the interaction between light and the free electron. The recurrence relation Eq. (S1.2), together with the initial condition $\psi_k^{(0)} = \delta_{k0}$, gives the following probability to absorb (or emit) k photons after N steps:

$$P_k = \left|\psi_k^{(N)}\right|^2 = |J_k(2|\beta|)|^2, \tag{S1.3}$$

where J_k is the Bessel function of the first kind of order k, and $|\beta| = |c|N$. This result proves the equivalence between the quantum walk theory and free-electron interaction with coherent-state light because Eq. (S1.3), obtained from the discrete step quantum walk, precisely matches Eq. (S2.27), obtained from the quantum theory of photo-induced nearfield electron microscopy (Q-PINEM) in Section S2 and Section S4 and in Refs. (*25-26*).

S1.2 The connection between the interaction of a free electron with thermal-state light to the random walk model

To model the electron interaction with thermal light, we adopt a similar approach to the previous section. However, instead complex number amplitudes, we consider classical probabilities. As before, a free electron can interact at each step with the thermal light in the following ways: (i) absorb a photon; (ii) emit a photon; (iii) no interaction. We consider the state of the electron to be described by a classical vector of probabilities:

$$P = (\dots, P_{-1}, P_0, P_1, \dots)^T, \tag{S1.4}$$

where P_k denotes the electron probability to be found in energy level $E_0 + k\hbar\omega$. Thus, Eq. (S1.4) is an analog of Eq. (S1.1) for random walk. After $n+1$ steps, the electron probabilities are described by:

$$P_k^{(n+1)} = (1-2p)P_k^{(n)} + pP_{k+1}^{(n)} + pP_{k-1}^{(n)}, \tag{S1.5}$$

where p is the probability to emit a photon. Eq. (S1.5) has the following solution if the initial conditions are $P_k^{(0)} = \delta_{k0}$:

$$P_k^{(N)} = e^{-2|\beta|^2} I_{|k|}(2|\beta|^2), \tag{S1.6}$$

where $|\beta|^2 = p \cdot N$. This result proves the equivalence between the random walk theory and free-electron interaction with thermal-state light because Eq. (S1.6), obtained from the discrete step random walk, precisely matches Eq. (S2.29), obtained from the Q-PINEM theory (*23, 25, 26*).

S1.3 The continuous transition from quantum to random walk

Sections S1.1 and S1.2 described the limits of random and quantum walk as models for the interaction of free electrons with light in thermal and coherent states, respectively. In this section, we consider the continuous transition between these two limiting cases.

To describe the continuous transition, we employ the following model. The light is assumed to be in a mixture of coherent and thermal states, assuming n_c photons from the coherent-state field, and n_{th} photons from the thermal field. We find that the order of interactions with the free electron does not alter the final electron energy spectrum. Thus, we calculate the interaction by first applying the coherent-state photons. After the interaction with n_c coherent photons according to Eq. (S1.3), the electron probability distribution of absorbing (or emitting) k photons is:

$$P_k = \left| J_k\left(2\frac{|\beta|}{N} n_c\right)\right|^2, \tag{S1.7}$$

This electron now interacts with n_{th} thermal photons according to Eq. (S1.5). The final electron energy spectrum is calculated numerically using Eq. (S1.7) as the initial condition.

Fig. S2 shows that the resulting electron energy spectrum precisely matches the full Q-PINEM calculation using the state of light of the amplifier theory Eq. (S4.1). Matching the theories involves defining a thermality parameter $r_{\mathrm{th}} \in [0,1)$, which we show to be connected to the amplifier gain and seed in Eq. (S4.2). The thermality r_{th} is defined in the following way:

$$\begin{cases} n_c = \sqrt{1-r_{\mathrm{th}}}N \\ n_{th} = r_{th}N \end{cases}, \tag{S1.8}$$

with $r_{\mathrm{th}} = 1$ giving pure thermal light, and $r_{\mathrm{th}} = 0$ giving pure coherent-state light.

To summarize this section, we showed a perfect match between free-electron interaction with light to the theory of quantum-to-random walk transition. Therefore, the theory of this section provides a simpler description for electron–light interactions in place of the rigorous Q-PINEM theory (Section S2), applied on the amplifier light (Section S3), and combined in Section S4.1.

S2. Interactions of free electrons with quantum light: the Q-PINEM theory

Here we discuss the quantum theory of the interaction between free electrons and quantum light (i.e., the theory of Q-PINEM). We discuss the implications of this general theory, such as electron–light entanglement, purity of the electron wave function, and the resulting electron energy loss spectra.

S2.1. A general theory of the Q-PINEM interaction

In this section, we formalize the free-electron-light interaction. According to Refs. (*23, 25, 26*), the scattering matrix of the interaction between free electrons and quantum light is described by:

$$S = \exp\left(g_{\mathrm{q}} b a^{\dagger} - g_{\mathrm{q}}^{*} b^{\dagger} a\right), \tag{S2.1}$$

where g_q is the quantum coupling constant, $b \equiv e^{-i\omega z/v}$, $b^{\dagger} \equiv e^{i\omega z/v}$ are the electron energy ladder operators, and a, $a^{\dagger}$ are the photonic annihilation and creation operators. The final state after the interaction can be written as:

$$\rho_{\mathrm{tot}}^{(\mathrm{f})} = S \rho_{\mathrm{tot}}^{(\mathrm{i})} S^{\dagger}\,, \tag{S2.2}$$

where $\rho_{\mathrm{tot}}^{(\mathrm{i})} = |E_0\rangle\langle E_0| \otimes \rho_{\mathrm{ph}}$. We define ρ_{ph} as the initial density matrix of the quantum light and $|E_0\rangle$ as the initial electron state with a well-defined energy E_0 (later, we will generalize it to an arbitrary initial electron state $\rho_{\mathrm{el}}^{(\mathrm{i})}$).

S2.2 The total density matrix following a Q-PINEM interaction

In this section, we calculate the joint density matrix of the electron and light $\rho_{\mathrm{tot}}^{(\mathrm{f})}$ and show the electron-light entanglement. We rewrite the scattering matrix Eq. (S2.1) as a Taylor series:

$$S = e^{\frac{|g_{\mathrm{q}}|^2}{2}} \sum_{m,l=0}^{\infty} \frac{\left(-g_{\mathrm{q}}^{*}\right)^m g_{\mathrm{q}}^{l}}{m!l!} (b^{\dagger}a)^m (b a^{\dagger})^l. \tag{S2.3}$$

We substitute Eq. (S2.3) into Eq. (S2.2), obtaining:

$$\rho_{\mathrm{tot}}^{(\mathrm{f})} = e^{|g_{\mathrm{q}}|^2} \sum_{n,n'=0}^{\infty} \rho_{\mathrm{ph}}(n,n') \sum_{m,l=0}^{\infty} \sum_{j,k=0}^{\infty} \frac{\left(-g_{\mathrm{q}}^{*}\right)^m g_{\mathrm{q}}^{l}}{m!l!} \frac{\left(-g_{\mathrm{q}}\right)^j g_{\mathrm{q}}^{*\,k}}{j!k!} a^m (a^{\dagger})^l |n\rangle \langle n'| a^k (a^{\dagger})^j$$
$$\otimes |E_0 + (m-l)\hbar\omega\rangle\langle E_0 + (j-k)\hbar\omega|, \tag{S2.4}$$

where $\rho_{\mathrm{ph}}(n,n') = \langle n|\rho_{\mathrm{ph}}|n'\rangle$ is the element of the photonic density matrix in the number basis. Using

$$\begin{cases} a^m (a^{\dagger})^l |n\rangle = \sqrt{\frac{(n+l)!}{n!}} \sqrt{\frac{(n+l)!}{(n+l-m)!}} |n+l-m\rangle \\ \langle n'| a^k (a^{\dagger})^j = \sqrt{\frac{(n'+k)!}{n'!}} \sqrt{\frac{(n'+k)!}{(n'+k-j)!}} \langle n'+k-j| \end{cases}, \tag{S2.5}$$

we find the total density matrix in terms of entangled electron–photon states

$$\rho_{\mathrm{tot}}^{(\mathrm{f})} = \sum_{n,n'=0}^{\infty} \rho_{\mathrm{ph}}(n,n') |\Psi_{\mathrm{el-ph}}^{n}\rangle\langle\Psi_{\mathrm{el-ph}}^{n'}|, \tag{S2.6}$$

where $\left|\Psi_{\mathrm{el-ph}}^{(n)}\right\rangle = \sum_{p=-\infty}^{\infty} \mathcal{C}_p^n |E_0 - p\hbar\omega\rangle|n+p\rangle$, and the coefficients are given by:

$$\mathcal{C}_p^n = e^{i\varphi_g p} \sum_{l=\max\{0,p\}}^{\infty} e^{\frac{1}{2}|g_{\mathrm{q}}|^2} \frac{(-1)^{l-p} |g_{\mathrm{q}}|^{2l-p}}{(l-p)!l!} \frac{(n+l)!}{\sqrt{n!(n+p)!}}.$$

We simplify further the expression for $\mathcal{C}_p^n$ and get:

$$\mathcal{C}_p^n = e^{i\varphi_g p} e^{\frac{1}{2}|g_\mathrm{q}|^2} \frac{|g_\mathrm{q}|^{|p|}}{|p|!} \begin{cases} \sqrt{\frac{(n+p)!}{n!}}\, {}_1F_1\left(1+n+p, 1+p, -|g_\mathrm{q}|^2\right), & p > 0 \\ (-1)^{|p|}\sqrt{\frac{n!}{(n-|p|)!}}\, {}_1F_1\left(1+n, 1+|p|, -|g_\mathrm{q}|^2\right), & p < 0 \end{cases}, \tag{S2.7}$$

where ${}_1F_1$ is the hypergeometric function. An equivalent representation of Eq. (S2.7) appears after the Eq. (4) in the main text.

We note that in the limit of weak interactions $|g_\mathrm{q}| \ll 1$, the coefficients $\mathcal{C}_p^n$ are simplified. Rearranging the terms, we get

$$\mathcal{C}_p^n = e^{i\varphi_g p} \sqrt{\frac{(n+p)!}{n^p n!}} \sum_{l=\max\{0,p\}}^{\infty} e^{\frac{1}{2}|g_\mathrm{q}|^2} \frac{(-1)^{l-p}|g_\mathrm{q}|^{2l-p}\sqrt{n^{2l-p}}}{(l-p)!l!} \frac{(n+l)!}{n^{l-p}(n+p)!}. \tag{S2.8}$$

For small $|g_\mathrm{q}| \ll 1$, the dominant contributions come from large n. In this limit, we obtain

$$\frac{(n+l)!}{n^{l-p}(n+p)!} \to 1, \ \sqrt{\frac{(n+p)!}{n^p n!}} \to 1, \ e^{\frac{1}{2}|g_\mathrm{q}|^2} \to 1,$$

such that

$$\mathcal{C}_p^n = e^{i\varphi_g p} \sum_{l=\max\{0,p\}}^{\infty} \frac{(-1)^{l-p}}{(l-p)!l!} \left(|g_\mathrm{q}|\sqrt{n}\right)^{2l-p} = e^{i\varphi_g p} J_p\left(2|g_\mathrm{q}|\sqrt{n}\right). \tag{S2.9}$$

Let's consider coherent-state light and show the absence of electron–photon entanglement for strong coherent-state light. In the case of coherent-state light, we have the following photon density matrix:

$$\rho_\mathrm{ph}(n, n') = e^{-|\alpha|^2} \frac{\alpha^n}{\sqrt{n!}} \frac{\alpha^{*n'}}{\sqrt{n'!}}, \tag{S2.10}$$

Since the density matrix in Eq. (S2.10) is separable in n and n', we can deduce that the total density matrix is a pure state:

$$\rho_\mathrm{tot}^{(\mathrm{f})} = |\Psi_\alpha\rangle\langle\Psi_\alpha|, \tag{S2.11}$$

where

$$|\Psi_\alpha\rangle = \sum_{p=-\infty}^{\infty} \left(\sum_{n=0}^{\infty} e^{-\frac{1}{2}|\alpha|^2} \frac{\alpha^n}{\sqrt{n!}} |n+p\rangle\right) \mathcal{C}_p^n |E_0 - p\hbar\omega\rangle. \tag{S2.12}$$

Hence, we showed that the interaction with coherent-state light leads to the completely pure state of the joint density matrix. However, Eq. (S2.12) shows that in the general case, there is entanglement between the electron and photon parts of the wavefunction, i.e., $|\Psi_\alpha\rangle$ cannot be decomposed into a tensor product of the two subsystem states. However, in the limit of small $|g_\mathrm{q}|$, we can substitute Eq. (S2.9) and get

$$|\Psi_\alpha\rangle = \sum_{p=-\infty}^{\infty} \left(\sum_{n=0}^{\infty} e^{-\frac{|\alpha|^2}{2}} \frac{\alpha^n}{\sqrt{n!}} |n+p\rangle\right) e^{i\varphi_g p} J_p\left(2|g_\mathrm{q}|\sqrt{n}\right) |E_0 - p\hbar\omega\rangle. \tag{S2.13}$$

For large $|\alpha|^2 \gg 1$, the distribution is narrowly peaked around $n \approx |\alpha|^2$, which allows us to write to a good approximation

$$|\Psi_\alpha\rangle = \sum_{p=-\infty}^{\infty} e^{i\varphi_g p} J_p\left(2|g_\mathrm{q}\alpha|\right) |E_0 - p\hbar\omega\rangle \otimes |\alpha\rangle, \tag{S2.14}$$

showing that in the semiclassical limit, the final joint electron–photon state is both pure and separable, i.e., not entangled.

Let's consider thermal light and show the emergence of electron–photon entanglement. The density matrix of the thermal state has the following diagonal form:

$$\rho_\mathrm{ph}(n, n') = \frac{1}{\langle n\rangle+1} \left(\frac{\langle n\rangle}{\langle n\rangle+1}\right)^n \delta_{n,n'}. \tag{S2.15}$$

Substituting the thermal density matrix Eq. (S2.15) into Eq. (S2.6), we get:

$$\rho_{\mathrm{tot}} = \sum_{n=0}^{\infty} \frac{1}{\langle n\rangle+1}\left(\frac{\langle n\rangle}{\langle n\rangle+1}\right)^{n} |\Psi_{\mathrm{e-ph}}^{(n)}\rangle\langle\Psi_{\mathrm{e-ph}}^{(n)}|, \tag{S2.16}$$

The state Eq. (S2.16) is not a pure state. Moreover, it cannot be separated into a tensor product of electron and light density matrices, i.e., it could contain electron–photon entanglement.

S2.3 The electron density matrix following the Q-PINEM interaction

In this section, we calculate the electron density matrix after a Q-PINEM interaction. The electron density matrix after the interaction equals to:

$$\rho_{\mathrm{el}} = \mathrm{Tr}_{\mathrm{ph}}\left[S\rho_{\mathrm{tot}}^{(\mathrm{i})}S^{\dagger}\right], \tag{S2.17}$$

where $\mathrm{Tr}_{\mathrm{ph}}$ is the trace with respect to the photonic degrees of freedom. We apply the photon trace-out on the total density matrix Eq. (S2.6-7), yielding the electron density matrix:

$$\rho_{\mathrm{el}}^{(\mathrm{f})} = \sum_{k=-\infty}^{\infty}\sum_{k'=-\infty}^{\infty} \underbrace{\left[\sum_{n=0}^{\infty}\rho_{\mathrm{ph}}(n+k,n+k')D_k^n D_{k'}^{n*}\right]}_{\rho_{\mathrm{el}}^{(\mathrm{f})}(k,k')} |E_0+k\hbar\omega\rangle\langle E_0+k'\hbar\omega|, \tag{S2.18}$$

where

$$\mathcal{D}_k^n = \frac{e^{\frac{|g_{\mathrm{q}}|^2}{2}}}{\sqrt{n!}} e^{-i\cdot\arg(g_{\mathrm{q}})k}\sum_{m=\max\{0,k\}}^{\infty}\frac{(n+m)!(-1)^m|g_{\mathrm{q}}|^{2m-k}}{\sqrt{(n+k)!}m!(m-k)!} = \mathcal{C}_{-k}^{n+k}. \tag{S2.19}$$

Note that in terms of the continuous free-electron energies E, E' measured in the experiment, the final electron density matrix can be expressed as the convolution of $\rho_{\mathrm{el}}^{(\mathrm{f})}(k,k')$ with $\rho_{\mathrm{el}}^{(\mathrm{i})}(E,E')$. The first part, defined in Eq. (S2.18) is a discrete electron energy comb with peaks that depend on the photon density matrix. The second part is the initial electron density matrix $\rho_{\mathrm{el}}^{(\mathrm{i})}(E,E')$, which includes its incoherent broadening and zero-loss peak from the process of electron photoemission at the tip. Together, we can write:

$$\rho_{\mathrm{el}}^{(\mathrm{f})}(E,E') = \rho_{\mathrm{el}}^{(\mathrm{i})}(E,E') * \sum_{k=-\infty}^{\infty}\sum_{k'=-\infty}^{\infty}\rho_{\mathrm{el}}^{(\mathrm{f})}(k,k')\delta(E-k\hbar\omega)\delta(E'-k'\hbar\omega). \tag{S2.20}$$

We use Eqs. (S2.19-20) to calculate the electron density matrix for different photonic states, as shown in Fig. S3 for different amplifier parameters (see also Section S3 for further details).

S2.4 Purity of the electron density matrix

This section investigates the purity of the electron state after the interaction to qualitatively estimate the entanglement between the initially pure electron and the light. The purity is defined as follows:

$$\mathrm{purity} = \frac{\mathrm{Tr}[\rho_{\mathrm{el}}{}^2]}{(\mathrm{Tr}\rho_{\mathrm{el}})^2} = \frac{\sum_{p,q}\rho_{\mathrm{el}}(p,q)\rho_{\mathrm{el}}(q,p)}{1} = \sum_{p,q}|\rho_{\mathrm{el}}(p,q)|^2. \tag{S2.21}$$

For coherent states, substituting Eq. (S2.10) into Eq. (S2.18), we get the electron density matrix:

$$\rho_{\mathrm{el}}(k,k') = \sum_n \mathcal{D}_k^n \mathcal{D}_{k'}^{n\,*} e^{-|\alpha|^2}\frac{\alpha^{n+k}\alpha^{*n+k'}}{\sqrt{(n+k)!}\sqrt{(n+k')!}} = \sum_n \mathcal{D}_k^n \mathcal{D}_{k'}^{n\,*}\underbrace{e^{-|\alpha|^2}\frac{|\alpha|^{2n}}{n!}}_{p(n)}\frac{n!\alpha^k\alpha^{*k'}}{\sqrt{(n+k)!}\sqrt{(n+k')!}}, \tag{S2.22}$$

For strong coherent-state light $|\alpha|^2 \gg 1$ and $|g_{\mathrm{q}}| \ll 1$, $p(n)$ is narrowly peaked around $n \approx |\alpha|^2$ such that:

$$\rho_{\mathrm{el}}(k,k') \approx \mathcal{D}_k^{|\alpha|^2}\left(\mathcal{D}_{k'}^{|\alpha|^2}\right)^{*}\frac{\Gamma(|\alpha|^2+1)\alpha^k\alpha^{*k'}}{\sqrt{\Gamma(|\alpha|^2+k+1)\cdot\Gamma(|\alpha|^2+k'+1)}} =$$

$$= \left(\mathcal{D}_k^{|\alpha|^2} \sqrt{\frac{\Gamma(|\alpha|^2+1)}{\Gamma(|\alpha|^2+k+1)}}\, \alpha^k \right) \cdot \left(\mathcal{D}_k^{|\alpha|^2} \sqrt{\frac{\Gamma(|\alpha|^2+1)}{\Gamma(|\alpha|^2+k'+1)}}\, \alpha^{k'} \right)^* . \quad \text{(S2.23)}$$

Hence, according to Eq. (S2.23), the final electron density matrix is separable:

$$\rho_{\mathrm{el}}(k,k') = \psi_{\mathrm{el}}(k)\psi_{\mathrm{el}}^*(k'), \quad \text{(S2.24)}$$

which implies purity of unity because

$$\text{purity} = \sum_{p,q} |\rho_{\mathrm{el}}(p,q)|^2 = \sum_{p,q} \rho_{\mathrm{el}}(p)\rho_{el}(q) = 1. \quad \text{(S2.25)}$$

This is in accordance with Eq. (S2.14), where we saw that the final electron–photon state is pure and separable.

In the case of the interaction with a thermal state, the initial density matrix of the photonic state is given by Eq. (S2.15). Hence, the density matrix of the electron according to Eq. (S2.18) is diagonal:

$$\rho_{\mathrm{el}}(k,k') = \delta_{k,k'} \sum_n \left| \mathcal{D}_p^n \right|^2 \frac{1}{\langle n \rangle + 1} \left(\frac{\langle n \rangle}{1+\langle n \rangle} \right)^{n+k}, \quad \text{(S2.26)}$$

showing that the density matrix is diagonal. According to Eq. (S2.26), the purity equals:

$$\text{purity} = \sum_{p,q} |\rho_{\mathrm{el}}(p,q)|^2 = \sum_k |\rho_{\mathrm{el}}(k,k)|^2 = \sum_k P_k^2, \quad \text{(S2.27)}$$

where P_k is the electron energy probability (as given for thermal light in Eq. (S2.32) below). Note that Eq. (S2.27) also holds for free-electron interaction with a Fock state.

In Fig. S4, we plot the purity of the final electron state following an interaction as a function of the interaction strength. In Section S4, the purity of the final electron state is plotted in Fig. S8 as a function of amplifier parameters, showing the transition from coherent to thermal states of light.

S2.5 Analysis of the diagonal elements of the total density matrix and quantifying the electron–light entanglement

According to Eq. (S2.4) and according to Ref. (*23*), the diagonal elements of the total density matrix following the Q-PINEM interaction $P_{nk} \equiv (\langle n| \otimes \langle E_0 + k\hbar\omega|)\rho_{\mathrm{tot}}^{(\mathrm{f})}(|E_0 + k\hbar\omega\rangle \otimes |n\rangle)$ are:

$$P_{nk} = \begin{cases} \left|g_{\mathrm{q}}\right|^{2k} e^{\left|g_{\mathrm{q}}\right|^2} \frac{(n+k)!}{(k!)^2 n!} \left| {}_1F_1\left(n+k+1, k+1, -\left|g_{\mathrm{q}}\right|^2\right)\right|^2 p_{n+k}, & k > 0 \\ \left|g_{\mathrm{q}}\right|^{2|k|} e^{\left|g_{\mathrm{q}}\right|^2} \frac{n!}{(k!)^2 (n-|k|)!} \left| {}_1F_1\left(n+1, |k|+1, -\left|g_{\mathrm{q}}\right|^2\right)\right|^2 p_{n-|k|}, & k < 0 \end{cases}, \quad \text{(S2.28)}$$

where p_n is the probability of the light to have n photons (satisfying $p_n = \sum_k P_{nk}$). In the case of large average number of photons $\langle n \rangle \gg 1$ and weak interaction $\left|g_{\mathrm{q}}\right| \ll 1$, Eq. (S2.28) can be simplified to:

$$P_{nk} = \left| J_{|k|}\left(2\left|g_q\right|\sqrt{n+k}\right)\right|^2 \cdot p_{n+k}. \quad \text{(S2.29)}$$

We use the following formula to quantify the light–electron correlations (plotted in Fig. S5):

$$\text{correlations} \equiv \sum_{n,k} |P_{nk} - p_n P_k|, \quad \text{(S2.30)}$$

where $P_k = \sum_n P_{nk}$ is the probability of the electron to absorb k photons. If the joint state has vanishing correlations, it means that the state is separable and does not contain any entanglement between the electron and photons. For correlations > 0, the state could be entangled, and Eq. (S2.30) provides an estimate for how strong the entanglement is. In Fig. S5, we plot the correlations of the final joint state for two cases: interaction with coherent- and thermal-state light as a function of the interaction strength. As can be seen in the figure, the coherent state interaction creates weak correlations, while for the thermal state interaction, the correlations are strong. This result explains

the conclusions in the main text about the role of photon statistics in creating quantum correlations and altering the eventual electron energy spectrum.

S2.6 Analysis of the diagonal elements of the electron density matrix and predictions for the measured electron energy spectrum

The diagonal elements of the electron density matrix, according to Eq. (S2.21), equals (*23*):

$$P_k = \begin{cases} \mathrm{Tr}\left[\rho_{\mathrm{ph}} \cdot \left|g_{\mathrm{q}}\right|^{2k} e^{|g_{\mathrm{q}}|^2} \frac{\hat{n}!}{(k!)^2(\hat{n}-k)!} \left|{}_1F_1\left(\hat{n}+1, k+1, -\left|g_{\mathrm{q}}\right|^2\right)\right|^2\right], \ k > 0 \\ \mathrm{Tr}\left[\rho_{\mathrm{ph}} \cdot \left|g_{\mathrm{q}}\right|^{2|k|} e^{|g_{\mathrm{q}}|^2} \frac{(\hat{n}+|k|)!}{(|k|!)^2 n!} \left|{}_1F_1\left(\hat{n}+|k|+1, |k|+1, -\left|g_{\mathrm{q}}\right|^2\right)\right|^2\right], k < 0 \end{cases}. \quad \text{(S2.31)}$$

In the case of $\langle n\rangle \gg 1$ and $\left|g_{\mathrm{q}}\right| \ll 1$, we can simplify Eq. (S2.31):

$$P_k = \sum_n \left|J_k\left(2\left|g_{\mathrm{q}}\right|\sqrt{n+k}\right)\right|^2 p_{n+k}. \quad \text{(S2.32)}$$

The coherent state has the following statistics:

$$p_n = e^{-\langle n\rangle} \frac{\langle n\rangle^n}{n!}, \quad \text{(S2.33)}$$

where the average number of photons equals $\langle n\rangle = |\alpha|^2$. Substituting Eq. (S2.33) into Eq. (S2.32), we approximately get for $g_{\mathrm{q}} \ll 1$:

$$P_k \approx \left|J_{|k|}(2|g|)\right|^2, \quad \text{(S2.34)}$$

where $|g| = \left|g_{\mathrm{q}}\right|\sqrt{\langle n\rangle}$.

The thermal statistics has the following form:

$$p_n = \frac{1}{1+\langle n\rangle}\left(\frac{\langle n\rangle}{1+\langle n\rangle}\right)^n. \quad \text{(S2.35)}$$

Substituting Eq. (S2.35) into Eq. (S2.32), we get the following electron energy spectrum:

$$P_k = e^{-2|g|^2} I_{|k|}(2|g|^2), \quad \text{(S2.36)}$$

where again $|g| = \left|g_{\mathrm{q}}\right|\sqrt{\langle n\rangle}$. The electron energy spectrum is calculated according to Eq. (S2.34) and Eq. (S2.36) and plotted in Fig. S6.

S2.7 Quantum weak measurement of photonic states using free electrons

In this section, we consider how the electron affects the light during its interaction. We calculate the quantum fidelity, which shows when the electron can be understood as a probe performing quantum weak measurement of the state of light.

We consider the light as our system and the free electron as the measurement device (pointer). The final joint state following the interaction is described by Eqs. (S2.6-7). Our pointer (electron) is measured strongly, i.e., projected on a specific energy value $M = |E'\rangle\langle E'|$, giving the final joint state

$$M\rho_{\mathrm{tot}}^{(\mathrm{f})} M = \rho_{\mathrm{ph}}^{(k)} \otimes |E'\rangle\langle E'|. \quad \text{(S2.37)}$$

Therefore, the act of measurement is a detection of a certain k^{th} electron energy peak. As in the previous sections, we use the index $k = \frac{E'-E}{\hbar\omega}$ to represent the discretized electron energy change, with $k > 0$ corresponding to subtraction of photons from the field. The density matrix of the

photonic system $\rho_{\mathrm{ph}}^{(k)}$ following the measurement can be written in a closed-form expression when considering a weak interaction ($|g_{\mathrm{q}}| \ll 1$) using Eq. (S2.9):

$$\rho_{\mathrm{ph}}^{(k)} = \frac{1}{N^{(k)}} \sum_{n=0}^{\infty} \sum_{n'=0}^{\infty} \rho_{\mathrm{ph}}(n+k, n'+k) J_k\left(2|g_{\mathrm{q}}|\sqrt{n+k}\right) J_k\left(2|g_{\mathrm{q}}|\sqrt{n'+k}\right) |n\rangle\langle n'|. \quad \text{(S2.38)}$$

The normalization factor $N^{(k)}$ is

$$N^{(k)} = \sum_{n=0}^{\infty} \rho_{\mathrm{ph}}(n+k, n+k) J_k^2\left(2|g_{\mathrm{q}}|\sqrt{n+k}\right) = \sum_{n=0}^{\infty} p_{n+k} J_k^2\left(2|g_{\mathrm{q}}|\sqrt{n+k}\right). \quad \text{(S2.39)}$$

To quantify what is considered as a quantum weak measurement, we calculate the fidelity F_k between the state of the light $\rho_{\mathrm{ph}}^{(k)}$ after the measurement and its initial state ρ_{ph}. Weak measurement is defined by fidelity F_k that approaches unity (*55*):

$$F_k = \left[\mathrm{tr}\sqrt{\sqrt{\rho_{\mathrm{ph}}}\rho_{\mathrm{ph}}^{(k)}\sqrt{\rho_{\mathrm{ph}}}}\right]^2 \to 1, \quad \text{(S2.40)}$$

In Fig. S7, we plot the fidelities F_k for different quantum optical states (coherent state, thermal state, and Fock state). For a coherent state of many photons with a small g_{q}, the measurement is always weak, whereas for the Fock state, it is always strong, except for the case of post-selection on $k = 0$. For a thermal state, the fidelity is lower than with a coherent state and decays more quickly for larger $|k|$. Interestingly, the fidelity of the measured coherent state is a symmetric around $k = 0$. The reason for this behavior stems from the fundamental difference between photon numbers subtracted and photon number added coherent states (*89*), which follow substantially different photon statistics. For photon subtraction ($k > 0$), the state is retained, whereas for photon addition ($k < 0$), the state changes more strongly. Still, both cases undergo a smaller change relative to the interaction with a thermal state. For a thermal state, the fidelity reduces substantially for both photon subtraction and addition in a rather symmetric fashion. Obviously, for the Fock state, adding or subtracting even just one photon completely changes the state, and the fidelity vanishes for all $k \neq 0$.

S3. Quantum optical properties of amplifier light: theory and analysis of the amplifier

In this section, we analyze the quantum properties of the light created by an amplifier.

S3.1. Quantum optical analysis of an amplifier model

To calculate the photon statistics in our experiment, we model our amplifier as a traveling-wave gain medium. This approach is a standard method to analyze a variety of amplifying gain media, such as fiber amplifiers. We denote the input field as a_{in}, the noise field by $b_{\mathcal{N}}$, and the amplifier gain by $\mathcal{G} > 1$. The output field is then given as (*5*):

$$a_{\mathrm{out}} = \sqrt{\mathcal{G}} a_{\mathrm{in}} + \sqrt{\mathcal{G}-1} b_{\mathcal{N}}^{\dagger}. \quad \text{(S3.1)}$$

This corresponds to an effective two-mode squeezing operation of the form

$$S(r) = \exp\left[r a_{\mathrm{in}} b_{\mathcal{N}} - r a_{\mathrm{in}}^{\dagger} b_{\mathcal{N}}^{\dagger}\right], \quad \text{(S3.2)}$$

where the squeeze parameter r satisfies $\sqrt{\mathcal{G}} = \cosh r$. The initial state of the amplifier is modeled as a coherent-state input seed $|\alpha\rangle$ and a vacuum noise field $|0\rangle$ such that the initial state is $|\Psi_{\mathrm{i}}\rangle = |\alpha, 0\rangle$. Subsequently, the final state satisfies

$$|\Psi_{\mathrm{f}}\rangle = S(r)|\alpha, 0\rangle = S(r) D_{\mathrm{in}}(\alpha)|0,0\rangle, \quad \text{(S3.3)}$$

with $D_{\mathrm{in}}(\alpha)$ denoting a displacement operator of the input field mode. We can exchange the order of the displacement and squeeze operator to have (*90*):

$$|\Psi_{\mathrm{f}}\rangle = D_{\mathrm{in}}(\alpha\cosh r)D_{\mathcal{N}}(-\alpha^{*}\sinh r)S(r)|0,0\rangle, \tag{S3.4}$$

where now, $D_{\mathcal{N}}(\alpha)$ is a displacement operator in the noise field.

We need to trace out the noise field if we want to find the state of the output field. Tracing out one mode of the two-mode squeezed coherent state given in Eq. (S3.4) yields a displaced thermal state for the output field, given by the Glauber P -function (*91*), which is a function of a complex number β

$$P(\beta) = \frac{1}{\pi(\mathcal{G}-1)}\exp\left[-\frac{(\beta-\sqrt{\mathcal{G}}\alpha)^{2}}{\mathcal{G}-1}\right]. \tag{S3.5}$$

From the P-function we can calculate the probability distribution by integrating over the complex plane $p_n = \int d^2\beta\ P(\beta)e^{-|\beta|^2}|\beta|^{2n}/n!$, yielding

$$p_n = e^{-|\alpha|^2}\frac{1}{\mathcal{G}}\left(1-\frac{1}{\mathcal{G}}\right)^{n} L_n\left(-\frac{|\alpha|^2}{\mathcal{G}-1}\right), \tag{S3.6}$$

where $L_n(x)$ is the n-th Laguerre polynomial. According to Eq. (S3.6), the photon statistics is described by α, the coherent amplitude of the input seed and $\mathcal{G} = \mathcal{G}(|\alpha|^2)$, the gain function of the amplifier, which is defined as the ratio between the output and input power (shown below in Fig. S10D). We use these two parameters, α and $\mathcal{G}$, to characterize the regime of operation of the amplifier. This way, the fitting enables us to extract the amplifier gain curve $\mathcal{G} = \mathcal{G}(|\alpha|^2)$.

For a weak seed $|\alpha|^2 \ll 1$ and $\mathcal{G} \gg 1$, we obtain the expected limit of a thermal state. In the other limit, a coherent-like state with Poissonian statistics is obtained for a saturated amplifier with an amplification $\mathcal{G}$, and an average number of photons of the input seed $\langle n_{\mathrm{in}}\rangle = |\alpha|^2 \gg 1$. In between, we obtain a range of states with super-Poissonian statistics, which span the entire range from thermal to the Poissonian statistics of coherent states. This situation can also be viewed in the following manner: when the amplifier is in the linear regime, the added noise has pure thermal statistics. The noise dominates the output light for a very weak seed. For a larger seed $|\alpha|^2 \gg 1$, the amplifier saturates. The added noise spectral density reduces substantially (*51*), and the amplifier noise statistics changes (*50*). However, the signal to noise ratio is very large, so the Poissonian statistics of the amplified signal dominates, and a coherent-like state is obtained, i.e., the statistics is Poissonian even if not always having the same degree of coherence as an ideal coherent state. In between, the added noise has contributions from the modified amplifier noise statistics and from the Poissonian amplified signal so that the resulting noise exhibits a transition from thermal to Poissonian statistics that is determined by $|\alpha|^2$.We now consider the limiting cases of the coherent-like and the thermal states in more detail.

The limit of amplified coherent-state light:

Let us consider the case $|\alpha|^2 \gg 1$ and saturated $\mathcal{G}$. In this case, Eq. (S3.6) has Poissonian statistics:

$$p_n \approx e^{-\langle n\rangle}\frac{\langle n\rangle^{n}}{n!}, \tag{S3.7}$$

where $\langle n\rangle \approx \mathcal{G}\cdot|\alpha|^2$. This equation completely coincides with the statistics of coherent-state light given by Eq. (S2.33).

The limit of amplified spontaneous emission (ASE), creating thermal light:

Let us consider a completely different case $|\alpha|^2 \ll 1$ and $\mathcal{G} \gg 1$. In this case, the statistics of Eq. (S3.6) can be simplified in the following way:

$$p_n = \frac{1}{\langle n\rangle+1}\left(\frac{\langle n\rangle}{\langle n\rangle+1}\right)^{n}, \tag{S3.8}$$

where $\langle n\rangle \approx \mathcal{G}-1$. This equation completely coincides with the statistics of thermal light given by Eq. (S2.35).

The general case:

We now consider the general case between thermal and coherent states of light and find the average number of photons and the second-order correlation $g^{(2)}(0)$ for the amplifier:

$$\langle n_{\mathrm{out}}\rangle = \mathcal{G}\cdot\langle n_{\mathrm{in}}\rangle + \mathcal{G} - 1, \tag{S3.9}$$

$$g^{(2)}(0) = 2 - \left(\frac{\mathcal{G}\cdot\langle n_{\mathrm{in}}\rangle}{\mathcal{G}\cdot\langle n_{\mathrm{in}}\rangle+\mathcal{G}-1}\right)^2, \tag{S3.10}$$

In the experiment presented in Fig. 3 from the main text, we kept the output power fixed (using an attenuator for the output light), while we increased the input number of photons. In the case of $\mathcal{G} \gg 1$, we can rewrite $g^{(2)}(0)$:

$$g^{(2)}(0) = 2 - \left(\frac{\langle n_{\mathrm{in}}\rangle}{\langle n_{\mathrm{in}}\rangle+1-\mathcal{G}^{-1}}\right)^2 \approx 2 - \left(\frac{\langle n_{\mathrm{in}}\rangle}{\langle n_{\mathrm{in}}\rangle+1}\right)^2. \tag{S3.11}$$

The $\langle n_{\mathrm{out}}\rangle$ and $g^{(2)}(0)$ as a function of $\langle n_{\mathrm{in}}\rangle$ are shown in Fig. S8 and in Fig. 3 of the main text.

We can also calculate the purity of the final electron density matrix, following its Q-PINEM interaction with the amplifier light, as a function of the amplifier gain $\mathcal{G}$. For that, we substitute the general photonic density matrix of the amplifier output (see Section S3.4 below) into Eq. (S2.18). The results of the calculation are depicted in Fig. S9.

S3.2. Analysis of the amplification curve and optical spectra

In addition to the Q-PINEM measurement, we reconstruct the statistics of the amplifier output using the following two optical methods: 1) Using the optical spectra (Fig. S10A); 2) Using the measured amplification curve (Fig. S10D), knowing both the power of the input light and the amplification coefficient $\mathcal{G}$. Let us focus on the first method. The typical optical spectra are shown in Fig. S11: it has some level of background noise, amplified noise, and a coherent peak due to the amplified input seed. The amplified noise spectrum has a rectangular shape due to the filter used in the experiment.

To analyze the amplifier statistics from the spectrum, we model the coherent-state input seed using a Gaussian spectral shape:

$$\frac{d\langle n_{\mathrm{in}}(\lambda)\rangle}{d\lambda} = I_0\, e^{-\frac{(\lambda-\lambda_0)^2}{\sigma^2}}, \tag{S3.12}$$

where $\lambda_0 = 1064$ nm and σ are defined by the bandwidth of the laser. The amplifier output signal is the sum of the three components: 1) amplified coherent-state input Eq. (S3.12); 2) amplified thermal noise, which is created due to the amplified spontaneous emission (ASE); 3) background noise. For $\mathcal{G} \gg 1$, the output can be expressed as

$$\frac{d\langle n_{\mathrm{out}}(\lambda)\rangle}{d\lambda} = \mathcal{G}(\omega) I_0\, e^{-\frac{(\lambda-\lambda_0)^2}{\sigma^2}} + \mathcal{G}(\omega)\cdot \mathrm{noise} + \mathrm{background\ noise}.$$

According to this model, we can extract $\mathcal{G}(\omega)$ (up to the multiplication constant) from examining the amplification of the noise relative to the unamplified part of the spectrum. Therefore, the value marked as G in Fig. S11 is proportional to the theoretical amplifier gain $\mathcal{G}$; we use it to find the amplification. Furthermore, the height of the Gaussian peak relative to the amplified noise is proportional to the input seed photon number $\langle n_{\mathrm{in}}\rangle$, so we could also use this scaling to find the amplification.

By either analyzing the measured amplification curve (option 1) or the optical spectra (option 2) of the output light, we can estimate the statistical properties of the amplifier output. The results of this analysis are shown in Fig. S10, where green points show the analysis based on the amplifier curve, red points denote the analysis of the optical spectra, and they are both compared with black

dots that represent the extracted gain from the electron measurement. The latter is explained in Section S4, detailing the method of analyzing the photon statistics based on the electron energy spectra resulting from the Q-PINEM interaction. The results from this method agree with the photon statistics obtained by the two previous methods (Fig. S10E).

S3.4. Density matrix description of the amplifier output in the photon number basis

In this section, we derive the photon density matrix of the amplifier output in the photon number basis. According to Eq. (S3.5), the density matrix of the amplified light is:

$$\rho_{\mathrm{ph}} = \int d^2\beta \, \frac{1}{\pi(\mathcal{G}-1)} \exp\left[-\left|\beta - \sqrt{\mathcal{G}}\alpha\right|^2/(\mathcal{G}-1)\right] |\beta\rangle\langle\beta|. \tag{S3.13}$$

To convert the density matrix to the photon number basis, we need to solve the following integral:

$$\rho_{\mathrm{ph}}(n,n') = \int d^2\beta \, \frac{1}{\pi(\mathcal{G}-1)} \exp\left[-\frac{\left|\beta-\sqrt{\mathcal{G}}\alpha\right|^2}{\mathcal{G}-1}\right] e^{-|\beta|^2} \frac{\beta^n}{\sqrt{n!}} \frac{\beta^{*n'}}{\sqrt{n'!}}. \tag{S3.14}$$

This is a two-dimensional Gaussian integral. The integral Eq. (S3.14) can be evaluated explicitly as:

$$\rho_{\mathrm{ph}}(n,n') = \frac{\alpha^{*n'-n}}{\mathcal{G}} \left(\frac{1}{\sqrt{\mathcal{G}}}\right)^{n'+n} \sum_{m=\max\{0,n-n'\}}^{n} \frac{\sqrt{n!n'!}}{(m+n'-n)!} \frac{(\mathcal{G}-1)^{n-m}}{(n-m)!} \frac{\exp(-|\alpha|^2)|\alpha|^{2m}}{m!}. \tag{S3.15}$$

Eq. (S3.15) gives the entire photon density matrix of the amplified light. We note that, as expected, the diagonal $\rho_{\mathrm{ph}}(n,n) = p_n$ recovers the statistics of Eq. (S3.6).

S4. Free-electron interaction with amplified light: Q-PINEM theory and fit to experiments

S4.1 Applying the Q-PINEM theory for the case of amplifier light

In this section, we revisit derivations from Sections 2 and 3 to explain how our electron–light interaction theory applies to the quantum statistics of photons created from the amplifier theory. Combining these results, we develop the full theory that we later fit to the experimental measurements. According to Eq. (S3.6) and Eq. (S2.32), the electron energy spectra after the interaction with amplified light are described by:

$$P_k = \sum_n \left|J_{|k|}\left(2\left|g_{\mathrm{q}}\right|\sqrt{n}\right)\right|^2 e^{-|\alpha|^2} \frac{1}{\mathcal{G}} \left(1-\frac{1}{\mathcal{G}}\right)^n L_n\left(-\frac{|\alpha|^2}{\mathcal{G}-1}\right), \tag{S4.1}$$

where the spectrum depends on two values: $|\alpha|$ and $\mathcal{G} = \mathcal{G}(|\alpha|^2)$. Eq. (S4.1) generalizes both the interaction with coherent-state light and with thermal light. In these limiting cases, the electron energy spectra are given by Eq. (S2.34) and Eq. (S2.36), respectively.

To capture the transition between thermal and coherent states, we recall the thermality parameter $r_{\mathrm{th}} \in [0,1)$ that arises from the ratio of the effective number of "thermal photons" to the total number of photons (Section S1.3). Thus, we define r_{th} as the ratio between the amplifier output without seed to the amplifier output with seed; using Eq. (S3.9), we get:

$$r_{\mathrm{th}} = \frac{\mathcal{G}-1}{\mathcal{G}\cdot|\alpha|^2+\mathcal{G}-1}. \tag{S4.2}$$

We can calculate the electron energy spectrum as a function of r_{th} using Eq. (S4.1) and Eq. (S4.2) for a fixed amplifier output power, i.e., a fixed $|g| = \left|g_q\right|\sqrt{\mathcal{G}\cdot|\alpha|^2+\mathcal{G}-1}$. These electron energy spectra are shown in Fig. S2 and are the same as the spectra calculated by the walker theory presented in Section S1, using Eq. (S4.2) and Eqs. (S1.7-8).

S4.2 Fitting of the experimental data

In this section, we compare the results obtained in the experiment with the theory. We extract the parameters $|\alpha|^2$ and $\mathcal{G}$ by fitting the measured electron energy spectra to Eq. (S4.1). We note that the photon statistics can be more generally extracted from the electron energy spectrum without employing the special case of the amplifier output. This procedure is described in Ref. (*23*).

Consider the experimental electron energy spectra in Fig. S12A. We want to compare it to the theoretical prediction of Fig. S12B, calculated according to Eq. (S4.1). To do this, we need to consider the fact that the initial electron is not monoenergetic and that there is an interaction between the free electron and the nanostructure, even in the absence of light. This interaction is due to the continuum of modes into which the electron emits spontaneously – which is exactly the effect of electron energy loss spectroscopy (EELS). To take this phenomenon into account empirically, we perform EELS measurements on the nanostructure in the absence of incident light (Fig. S12C). We then use the measured EELS (Fig. S12C) to convolve the results of our single-mode Q-PINEM theory.

Altogether, to compare the theory Fig. S12B with the experimental Fig. S12A, we convolve the theoretical peaks with the experimentally obtained zero-loss peak (Fig. S12C), obtaining the final theoretical spectrum, as in Fig. S12D. To fit the model to the experimental data, we use two fitting parameters from the theory: $a = \eta\left|g_{\mathrm{q}}\right|^2\mathcal{G}$ and $b = \eta\left|g_{\mathrm{q}}\right|^2\mathcal{G}\langle n\rangle$, where η is the coupling efficiency of the light with the silicon-photonic nanostructure, i.e., the ratio between the number of photons that are coupled to the nanostructure and the number of photons emitted from the amplifier. In this manner, we fit the theory and experimental results in all the figures of the main text and extract the corresponding fit parameter values of $\eta\left|g_{\mathrm{q}}\right|^2\mathcal{G}$ and $\eta\left|g_{\mathrm{q}}\right|^2\mathcal{G}\langle n\rangle$ for the different experiments. Thus, for example, we can reconstruct the photon statistics in Fig. 3 from the main text. Moreover, we can calculate the strength of the quantum coupling constant $\sqrt{\eta}\left|g_{\mathrm{q}}\right| \approx 0.016$, extracting it from the fit parameter $a = \eta\left|g_{\mathrm{q}}\right|^2\mathcal{G}$, by using the gain $\mathcal{G}$ obtained from the amplification curve described in Section S3.

Fig. S13 presents the comparison between the experimental and the fitted theoretical spectra for different strengths of the electric field, shown for the limits of coherent and thermal states of light.

S4.3 The asymmetry in the measured electron energy spectra

Figs. 1C,D and Figs. 2A,B,D from the main text show an intrinsic asymmetry in the electron energy spectra. Such asymmetry arises from inelastic scattering of the electron by the structure, including spontaneous emission of a range of optical excitations (usually without phase-matching) (*90, 91*). This behavior contrasts with the symmetry of the rest of the features in the electron energy spectra, which all arise from stimulated emission and absorption. In principle, both spontaneous and stimulated effects can be fully captured by the QPINEM theory when applied to a continuum of optical modes (*66, 92*). However, the single-mode QPINEM theory that we employ (Eqs. (2-4) from the main text and Section S2) does not capture the asymmetry. Thus, we apply an empirical approach to capture the asymmetry of inelastic scattering: we measure the electron energy loss spectrum (EELS) (*92*) in the interaction with no external light illumination (Fig. S13), and then

we convolve it with the result of the QPINEM theory, showing good agreement with the experimental data.

Despite the free-electron interaction involving a continuum of optical modes, as seen by the asymmetric EELS (Fig. S13), the light excitation only couples to a single mode (the light bandwidth is narrow enough for the single-mode approximation being accurate). Consequently, the free-electron–light interaction acts as a probe of that single mode rather than of the continuum. Importantly, even when the light excitation is broadband and couples to a wider continuum of modes, quasi-phase-matching could enable selective probing of a single mode by tuning the electron velocity.

S4.4 Mechanisms other than photon statistics that alter the electron energy spectrum

We verify that our observed quantum-to-classical transition does not arise from the lack of spatial/temporal optical coherence. The spectral bandwidth of thermal light in our experiment (4 nm) depicts a longer temporal coherence (900 fs) than the electron–light interaction duration (410 fs). The transverse coherence of light is similarly longer than the electron–light interaction length (84 μm), as it is emitted from a single-mode fiber (6 μm core). Thus, optical coherence is fully maintained even for thermal light. To further strengthen this conclusion, we developed the theory for free-electron interaction with partially coherent light (Section S6). We find that partial optical coherence reduces the efficiency of quasi-phase-matching in a manner that no longer matches with our measurement due to the diminished interaction strength (Fig. S16 below in Section S6). In contrast, we find equal interaction strengths (variance in energy) for both coherent states and thermal states of the same intensity (e.g., white circles in Fig. 1C,D from the main text), implying the same level of optical coherence in both cases. We conclude that the differences in electron energy spectra for different states of light arise *entirely* from differences in photon statistics, leading to quantum decoherence in the energy domain (which can be equally understood in the language of collapse or entanglement).

It is also valuable to compare our measurements of free-electron–quantum-light interactions to previous work in PINEM. Fig. 1C from the main text exactly corresponds to the PINEM theory (*17,18*), showing quantum walk (also called Rabi oscillations in some works) first observed in Ref. (*14*). The difference is that our experiment observes this effect using CW light rather than a pulsed laser, which is orders of magnitude more intense. Fig. 1D from the main text exactly corresponds to the Q-PINEM theory with thermal light statistics, showing classical random walk, which has a Gaussian distribution. Certain PINEM experiments with coherent laser pulses (e.g., Ref. (*13*)) showed Gaussian-like distributions and may be mistakenly perceived as similar: Importantly, in these experiments, the Gaussian-like electron energy distributions arose from the inhomogeneous temporal field profile along the interaction with the electron (the electron pulse duration was longer than the laser pulse duration), and from the inhomogeneous spatial profile inside the electron beam diameter. In contrast, CW light maintains an average intensity $\langle I(t)\rangle = \langle I\rangle$ that does not depend on time and thus remains homogeneous along the interaction with the electron. Moreover, our electron beam diameter is small enough (Materials and methods) to eliminate spatial inhomogeneities. Hence, the effects we observe here are purely due to photon statistics.

S5. The phase-matching condition and its analysis

The requirement for a strong interaction between free electrons and extended light fields is matching the electron velocity with the light's phase velocity. This requirement is called the phase-matching condition in electron–light interactions. The phase-matching condition is well-known in classical electrodynamics and forms the basis of efficient dielectric laser accelerators (DLAs) (*8, 10*). This phase-matching condition was recently shown in a PINEM interaction, where the electron is a quantum wavefunction, and the light is a coherent state (*40*). In this section, we describe how the phase-matching condition arises in the PINEM theory and why it is directly applicable in Q-PINEM (*40, 92, 93*) for any form of quantum light.

The subsections below present how the phase-matching condition arises straightforwardly from the PINEM theory and then present its generalization to a quasi-phase-matching condition, which appears in our experiment. We use rigorous numerical simulations of the field inside the nanostructure to fully describe the interaction and compare it with the model arising from PINEM theory.

S5.1. The emergence of phase-matching from the PINEM theory

To find the phase-matching condition in the PINEM theory, let us calculate the strength of the PINEM interaction (see Ref. (*40*)):

$$|g| = \frac{e}{\hbar\omega}\left|\int E_z(z)e^{-i\frac{\omega}{v}z}dz\right|. \tag{S5.1}$$

The field $E_z(z)$ in the structure is given by:

$$E_z(z) = E_0 e^{ik_z z}, \tag{S5.2}$$

where $k_z = k_0 n\cos\theta$ is the projection of the wavevector on the z axis, $k_0 = 2\pi/\lambda_0$ is the wavenumber of the mode, and λ_0 is the wavelength. Substituting Eq. (S5.2) into Eq. (S5.1), we get:

$$|g| = \frac{e|E_0|}{\hbar\omega}\left|\int_{-L/2}^{+L/2}\exp(ik_0(n\cos\theta-\beta^{-1})z)\,dz\right|, \tag{S5.3}$$

where n is an effective refractive index, θ is the angle between the electron velocity (i.e., the z-axis) and the wavevector of the light, $\beta = v/c$ is the normalized velocity of the free electron, and L is an effective interaction length.

The integral in Eq. (S5.3) yields:

$$|g| = \frac{e|E_0|}{\hbar\omega}L\left|\mathrm{sinc}\left(\frac{k_0 L}{2}(n\cos\theta-\beta^{-1})\right)\right|, \tag{S.5.4}$$

The phase-matching condition then reads:

$$n\cos\theta-\beta^{-1}=0, \tag{S5.5}$$

and the phase-matched value of $|g|$ equals to:

$$|g|^{(\max)} = \frac{e|E_0|}{\hbar\omega}L. \tag{S5.6}$$

S5.2. Quasi-phase-matching in periodic structures: the inverse Smith–Purcell effect

The previous subsection can be understood as an implementation of the inverse Cherenkov effect, as shown in Ref. (*40*). Our experiment can be explained in an analogous manner as an implementation of the inverse Smith–Purcell effect.

In a periodic structure, the condition for a strong interaction of a free electron with light is called the quasi-phase-matching condition (in analogy to periodic-poled crystals in nonlinear optics). As

with other forms of free-electron–light phase-matching, this condition guarantees that the electron velocity is equal to the phase velocity of the optical mode of the light in the structure. Hence, the interaction strength is sensitive to the electron velocity and allows us to selectively couple the electron to (approximately) a *single mode of light*. Moreover, the quasi-phase-matching condition not only enhances the interaction with a chosen single mode but also suppresses the interaction with the other light modes. This way, we could choose a specific light wavelength by tuning the velocity of the electron (Section S5.4).

In the presence of a periodic structure with periodicity Λ, the field in Eq. (S5.1) is:

$$E_z(z) = \sum_m E_m e^{i\left(k_0 \cos\theta + \frac{2\pi}{\Lambda} m\right) z}, \tag{S5.7}$$

where m is the Fourier (diffraction) order of the mode with amplitude E_m. Then, the interaction strength becomes

$$|g| = \frac{e}{\hbar\omega} \left| \sum_m E_m \int_{-\frac{L}{2}}^{+\frac{L}{2}} \exp\left(i \left(k_0 \cos\theta + \frac{2\pi}{\Lambda} m - \frac{\omega}{v} \right) z \right) dz \right|. \tag{S5.8}$$

Usually, only one diffraction order m is phase matched, hence the coupling is simplified to

$$|g| = \frac{e|E_m|L}{\hbar\omega} \left| \mathrm{sinc}\, \pi L \left(\frac{1}{\lambda_0} \cos\theta + \frac{1}{\Lambda} m - \frac{1}{\lambda_0 \beta} \right) \right|, \tag{S5.9}$$

where we substituted $\lambda_0 = 2\pi/k_0$. Then, the phase-matching condition becomes

$$\lambda_0 = \frac{\Lambda}{m} (\beta^{-1} - \cos\theta), \tag{S5.10}$$

which is exactly the Smith-Purcell dispersion relation (*61*), describing the spontaneous emission of photons by electrons near a periodic structure. Therefore, our experiment implements the inverse Smith–Purcell effect, which was described theoretically with electron wavefunctions (*62, 63*), but so far never showed with CW light nor with non-Poissonian driving light.

S5.3. The analysis of experimental data

In this part of the section, we discuss the experimental verification of the phase-matching condition. Using the method suggested in Section S4 for each spectrum, we extract the coupling strength $|g|$ as a function of electron velocity. To analyze the phase-matching, we compared these experimental measurements with Eq. (S5.9). We substitute $\lambda_0 = 1064$ nm, $\Lambda = 733$ nm, $m = 1$, and $\theta = 90°$. Using the measured electron energy spectra as a function of electron velocity for interactions with coherent-state light (Fig. 5A from the main text, also Fig. S14 below), we fit the theory to the experimental results and find the effective interaction length with the structure: $L \approx 56$ μm.

The rigorous numerical simulation of the electromagnetic fields inside the structure gives a good agreement with the simple model described by Eq. (S5.9). Although the experimental results show an asymmetric behavior that partially deviates from the theory for high electron acceleration, they generally follow the same trend and have the same quasi-phase-matching condition. A more advanced theory could consider the transverse Gaussian profile and defects of the structure. Such theory can potentially provide a more precise fit capturing the asymmetric behavior of the data and the deviation from the theory for high electron velocities.

To summarize this section, we note that the idea of phase-matching between the electron wavefunction and the light wave can lead to strong coupling between free electrons and light. The phase-matching is sensitive to the phase velocity of the mode of light and to the electron velocity, and thus, it allows us to couple exactly to a *single mode of light*. The phase-matching condition not only enhances the interaction with a chosen single mode but also diminishes the interaction

with all the other light modes. In this manner, we can selectively couple to a selected light mode by tuning the velocity of the electron. The practical resolution by which the phase-matching condition enables to isolate a single mode is determined by the extent and duration of the interaction (in our case, it is 84 μm, which limits our wavelength resolution to about 8 nm).

S5.4. Detection of quantum light by using free electrons: prospects for extremely high resolution in both time and frequency

The quasi-phase-matching shown in Fig. S14 and also in Fig. 5 from the main text could provide a useful capability for quantum-optical detection: resolving the quantum photon statistics of an individual mode (single frequency) out of a multi-mode (or a spectrally broad) pulse of quantum light. By scanning over the electron velocity, as in Fig. 5 from the main text, we can select a particular mode with which the electron satisfies quasi-phase-matching. Then the interaction could potentially isolate the photon statistics of that mode. The spectral resolution improves for quasi-phase-matching of longer extent and duration (see Fig. S15). The maximum wavelength range that can be probed depends on the bandwidth of the nanostructure's spectral response, which is 8 nm in our case (Fig. 5D inset from the main text) and can be significantly wider (as already shown in previous work, e.g., Ref. (*94*)).

Another advantage of free-electron-based quantum-optical detection is the prospects of reaching time resolutions only limited by the electron pulse duration (*23*); currently, tens-hundreds of fs. These time resolutions are already better than all existing mechanisms of quantum light detection, which are limited by electronic timescales (*95*). Future work can improve the time resolution to attosecond timescales using attosecond electron combs (*19-21, 83*). Our free-electron-based approach can also be attractive for wide-bandwidth quantum-optical detection (*96, 97*), and potentially lift the bandwidth limitation from applications such as continuous-variable quantum information processing (*96*). As with all other components and detectors in quantum optics, the future success of our detection technique depends on high efficiency (low loss) manipulation of light; specifically, efficient coupling into the nanostructure that performs the electron–light interaction. High-efficiency coupling of light into silicon-photonic nanostructures is a topic of intense investigation and is already available as on-chip technology (*72*).

S6. The role of optical coherence in Q-PINEM interactions

In this section, we consider the model of interaction of free electrons with partially coherent light and show the effect of the partial optical coherence on the electron energy spectra. This analysis shows that partial optical coherence cannot explain our experimental data, and it must be due to the higher orders of coherence – i.e., the quantum photon statistics. We emphasize the distinct differences between effects of partial optical coherence and the effects of quantum statistics observed in our experiments (due to super-Poissonian and thermal light statistics).

We consider classical coherent light. According to Eq. (S5.1), the coupling between light and free electrons equals to:

$$g = |g|e^{i\phi} = \frac{e}{\hbar\omega}\int E_z(z)e^{-i\frac{\omega}{v}z}dz, \tag{S6.1}$$

where $E_z(z)$ is the classical electric field along the z axis. To model optically incoherent light, we consider consecutive interactions with N coherent fields, each with coherence length $l_c = L/N$ (L is the total interaction length) and a constant phase ϕ_i over this interval, where each phase is uniformly distributed in $[0,2\pi]$. This simple model gives the following coupling strength:

$$g = \frac{|g|}{N}\sum_{i=1}^{N} e^{i\phi_i}, \tag{S6.2}$$

The results of the numerical calculations of the electron energy spectra for different N values (i.e., different optical coherence lengths l_c, decreasing for larger N) are displayed in Fig. S16.

We find that for partial optical coherence of light, i.e., shorter coherence length l_c, the energy spread of the electron after the interaction decreases. In the language of quantum walk, this is equivalent to a quantum walk in a temporally disordered medium, resulting in the diffusion scaling linear but with a smaller slope, until eventual localization emerges (no energy spread). We can use the slope of the energy spread as the function of $|g|$ to identify the degree of optical decoherence. When applying this analysis to our experiment, we find that our data can be explained by fully coherent light, with no need for corrections due to partially incoherent light.

Importantly, this section shows that one cannot explain free-electron interactions with thermal light using partial optical coherence – these are two completely separated effects (one associated with phase fluctuations in the light, and the other with photon statistics – or intensity fluctuations). In our experiment, the thermal state had full optical coherence in both time and space. In time, the temporal coherence can be estimated from the bandwidth to be at least 900 fs, which is larger than the interaction duration with the electron, 410 fs. In space, the spatial coherence is longer than the structure length if 84 μm, since the light is emitted from a single mode fiber, the same one used for the coherent-state light.

S7. The interaction of classical point electrons with quantum light

In this section, we derive the interaction between a point free electron and quantum light for the case of coherent and thermal states of light. Here we should note that we use a rather exotic assumption: while we treat an electron as a point particle (completely ignoring its wave nature), we consider light as a quantum object. With this purpose, we calculate the electron energy spectrum for interaction with a classical electromagnetic field (i.e., for coherent states of light) and for the interaction with thermal light using the Glauber P-function. We use this derivation to compare with our fully quantum analysis (main text Fig. 3), showing that the quantum theory is necessary in all cases.

Coherent-state light can be described by a classical electromagnetic field $E_z(t)$. Thus, the interaction of the coherent-state light with an electron can be described by the following equation of motion:

$$m_e \frac{dv}{dt} = -e \cdot E_z(t), \tag{S7.1}$$

where m_e is the mass of the electron, e is the elementary charge, and v is the electron velocity. The magnetic term in Eq. (S7.1) is negligible in our conditions. We assume that the initial electron position is uniformly distributed over a single optical cycle of the electromagnetic field. Within these assumptions, it can be shown that the probability distribution over the energy of the electron after the interaction is (detailed derivation can be found in Ref. (*40*)):

$$P_{\text{coherent}}(\Delta E, \alpha) = \frac{1}{\pi\sqrt{4|g|^2(\hbar\omega)^2 - (\Delta E)^2}}, \tag{S7.2}$$

where ΔE is the electron energy shift, $|g|^2 = \left|g_{\text{q}}\right|^2 \cdot \langle n \rangle = \left|g_{\text{q}}\right|^2 |\alpha|^2$ is the number of photons in the coherent-state light, and ω is the frequency of the light. The formula in Eq. (S7.2) exactly corresponds to the acceleration in the classical theory of DLA. Fig. S17 (left) compares the classical theory with the quantum (PINEM) theory, showing that they do not match and that only the quantum theory matches with the experimental data.

We now calculate the interaction of a classical point electron with thermal light. The density matrix of thermal light according to Ref. (*4*) can be described by the Glauber function:

$$\rho_{\text{thermal}} = \int P(\alpha)|\alpha\rangle\langle\alpha| d^2\alpha, \tag{S7.3}$$

where $|\alpha\rangle$ is the coherent state of light, $P(\alpha) = \frac{1}{\pi\langle n\rangle} e^{-|\alpha|^2/\langle n\rangle}$ is the Glauber function of the thermal light, and $\langle n\rangle$ is the average number of photons. The resulting probability distribution of the electron energy shift equals to:

$$P_{\text{thermal}}(\Delta E) = \int P_{\text{coherent}}(\Delta E, \alpha) \cdot P(\alpha)\, d^2\alpha. \tag{S7.4}$$

Substituting Eq. (S7.3) into Eq. (S7.4), we get:

$$P_{\text{thermal}}(\Delta E) = \frac{1}{2\sqrt{\pi}|g|\hbar\omega} e^{-\left(\frac{\Delta E}{2|g|\hbar\omega}\right)^2}, \tag{S7.5}$$

where $|g|^2 = \left|g_{\text{q}}\right|^2 \cdot \langle n\rangle$. Fig. S17 (right) compares the classical theory and the quantum (Q-PINEM) theory, showing that they do not match in the thermal case either.

To summarize, this section presents an attempt at an alternative theory to explain the measurements. This alternative theory does not match with our data, which helps eliminate an explanation of our experiment as a "collapse" or "measurement" of the electron in space. If the thermal light could "measure" ("collapse") the position of the electron, i.e., localize the electron in space, then such a situation would correspond to the classical theory that we consider in this section. Instead, we find that the electron "collapse" only occurs in the energy domain and that such a quantum theory is the one that correctly matches the measured data. Therefore, our experiment demonstrates that we work in a quantum regime in which the electron wavefunction has a long coherence length (much larger than the wavelength of the light) and a long coherence duration (much longer than the optical cycle).

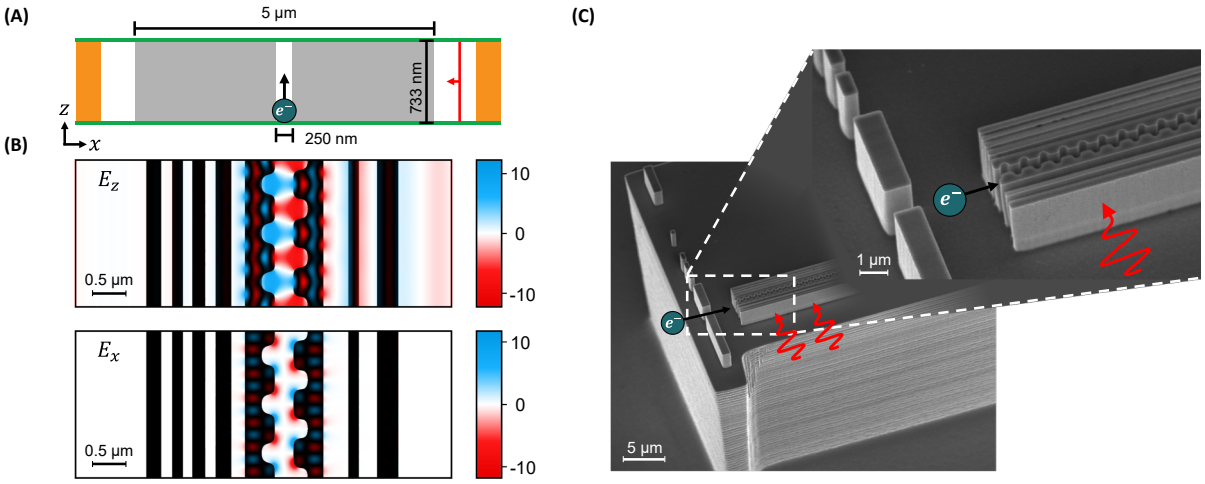

Fig. S1. Silicon-photonic nanostructures for efficient electron–light coupling: based on dielectric laser accelerators (DLAs). (A) Schematic illustration of the two-dimensional simulation cell used for inverse design. The nanostructure was optimized over a 5-µm-wide design region (grey) with a 250-nm-broad vacuum channel in the center. Periodic boundaries (green) were applied in the longitudinal direction, and perfectly matched layers (orange) were defined at the remaining boundaries. A transverse-magnetic plane wave (red) was excited on one side, and the resulting acceleration gradient, measured in the center of the channel, served as the objective function. **(B)** Electric field components E_z and E_x normalized by the incoming field amplitude. **(C)** SEM picture showing our DLA-type nanostructure on a 30-µm-high mesa.

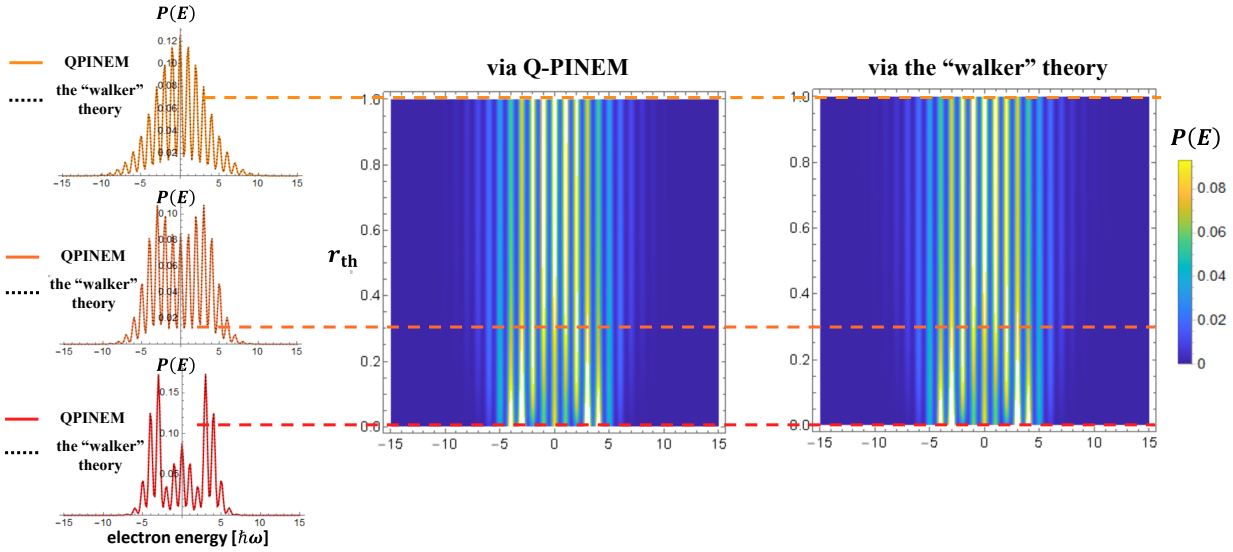

Fig. S2. Comparison between quantum-to-random "walker": theory and Q-PINEM theory, showing the equivalence of the two models. The electron energy spectra as a function of the thermality coefficient r_{th}, calculated for both theories and showing the exact match between the results predicted by these different theories.

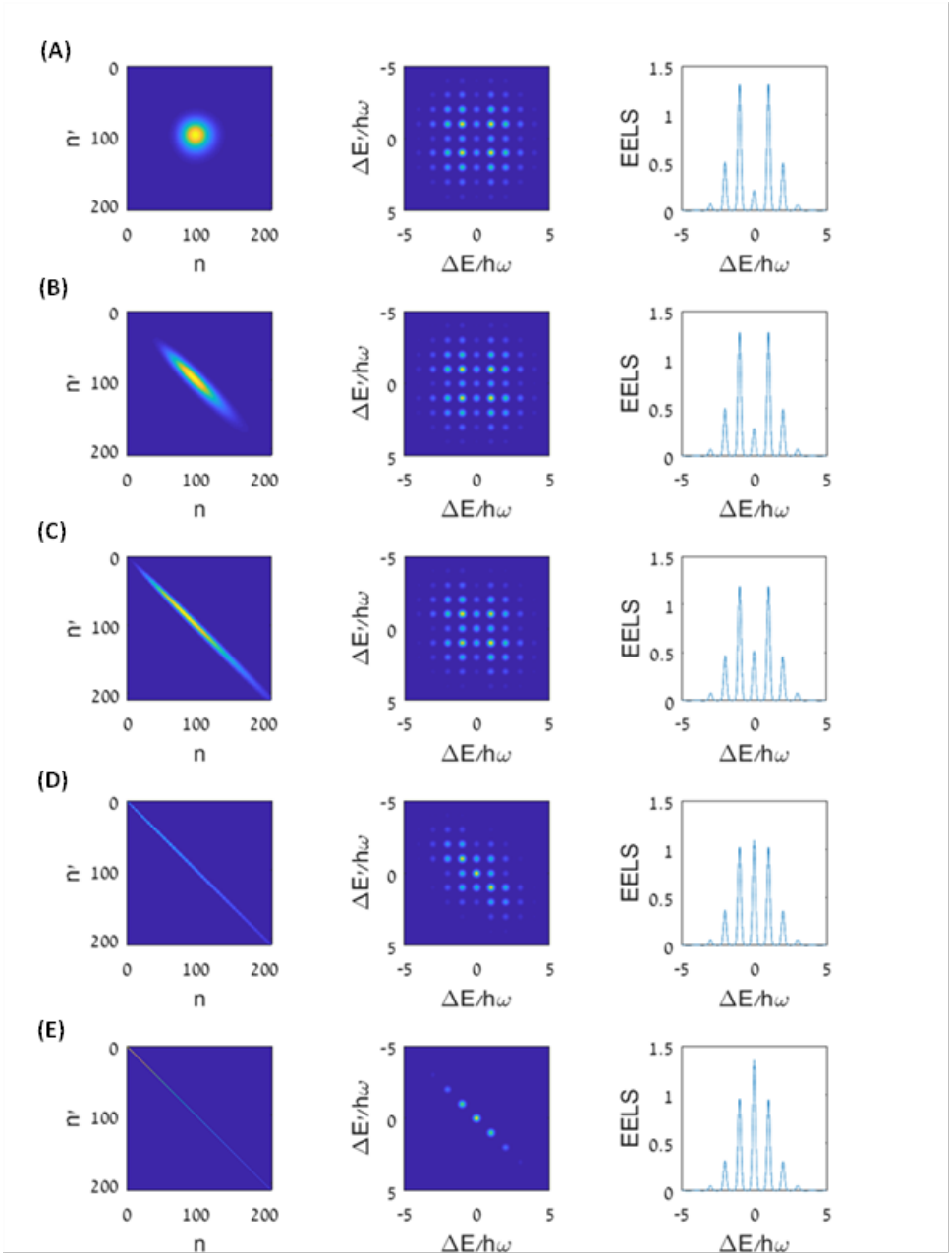

Fig. S3. Electron quantum state following a free-electron–light interaction. Left column: Initial photon density matrix (its absolute values) in the number basis. Middle column: Final electron density matrix (its absolute values) in energy space. Right column: Electron energy spectrum. For all examples, the average number of photons is $\bar{n} = 100$, the quantum coupling constant is $g_q = 0.1$, and the electron initial energy uncertainty is $\Delta E = 0.1\hbar\omega$. (A)-(E): Q-PINEM interaction with an initial photonic state from the amplifier output, ranging between coherent-state light to thermal light, for a chosen gain of **(A)** $G = 1$, **(B)** $G = 3.37$, **(C)** $G = 11.35$, **(D)** $G = 38.27$ and **(E)** $G = 101$. The photonic quantum state necessary for this calculation is developed in Section S3.5.

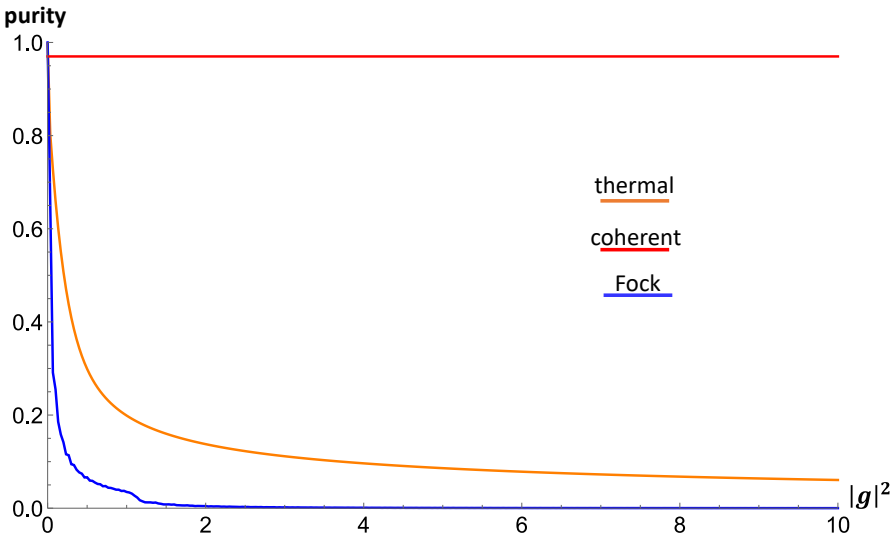

Fig. S4. Purity of the electron's final state following an interaction with different states of light, as a function of the interaction strength $|\boldsymbol{g}| \equiv |\boldsymbol{g}_{\mathbf{q}}|\sqrt{\boldsymbol{n}}$.

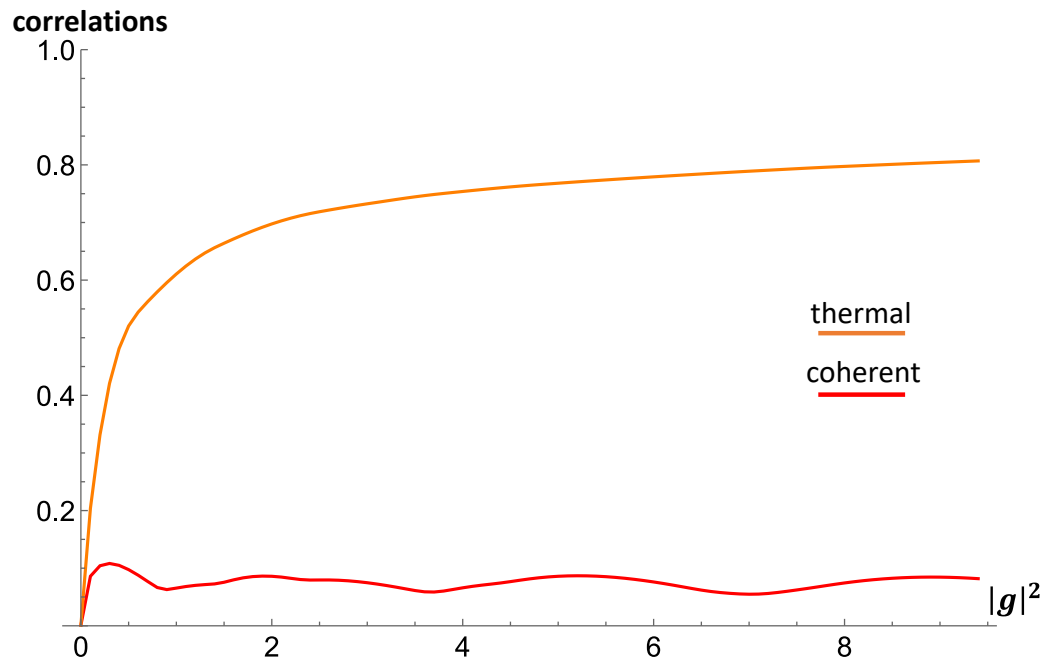

Fig. S5. Correlations between the light and the free electron showing their entanglement. The correlations are plotted for the interaction with coherent and with thermal light. We see that the thermal state creates stronger correlations with the electron than the coherent state. The curves are calculated for $|g_q| = 0.1$, using Eq. (S2.30).

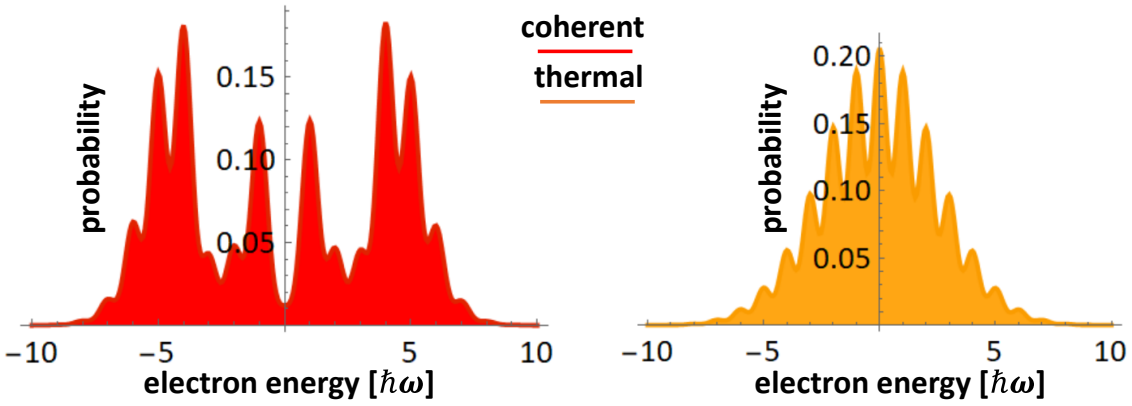

Fig. S6. Electron energy spectra for the interactions with coherent and thermal states of light, calculated according to Eq. (S2.34) and Eq. (S2.36).

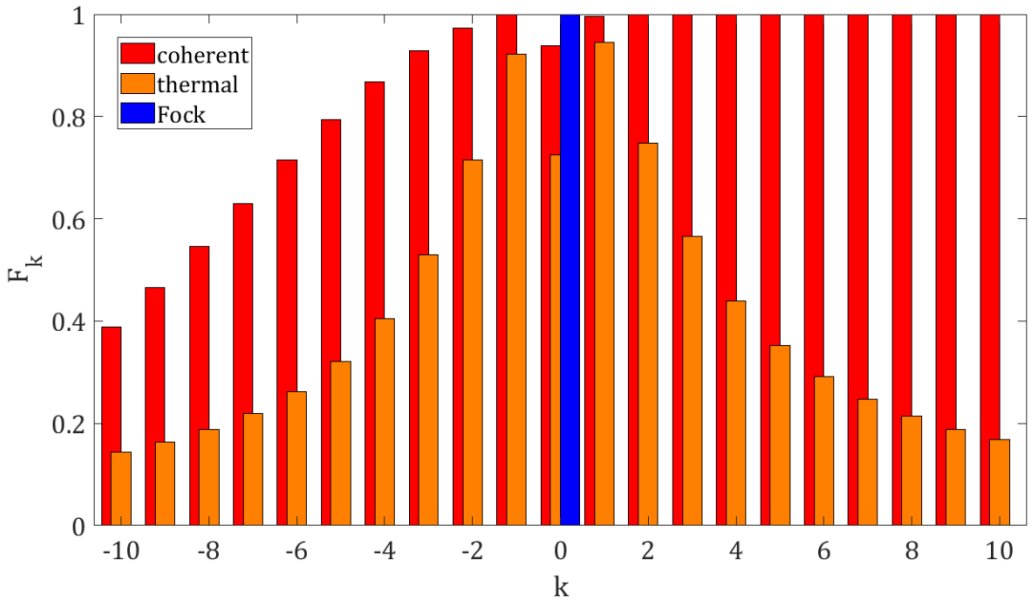

Fig. S7. Quantum weak measurement vs. projective measurement. The fidelity quantifies how much the photonic state changes due to the electron interaction. The bars show the fidelity of the photonic state (the measured system) following the detection of the electron (the measuring pointer) at the $\boldsymbol{k}$-th energy peak, for a coherent state (red), thermal state (orange), and a Fock state (blue). All curves are calculated with a mean photon number of $\langle \boldsymbol{n} \rangle = \mathbf{100}$ and $\boldsymbol{g_q} = \mathbf{0.1}$.

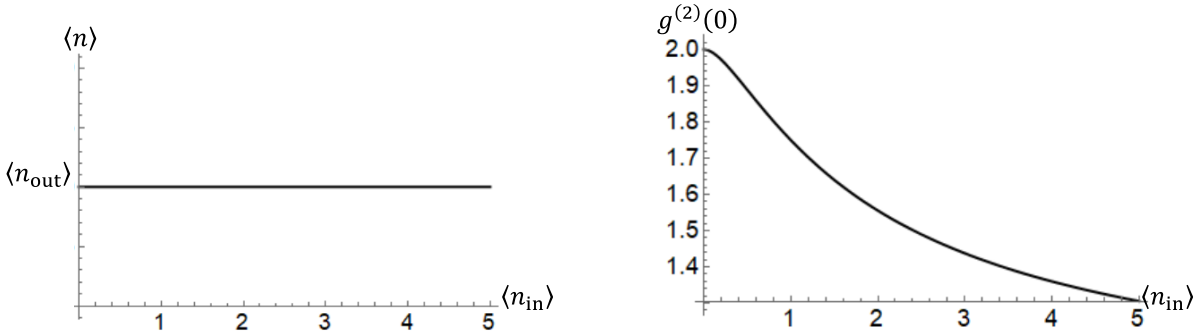

Fig. S8. Transition between coherent and thermal state for the amplifier output as a function of the input number of photons $\langle \boldsymbol{n}_{\mathbf{in}} \rangle$. The output power was kept fixed using an attenuator.

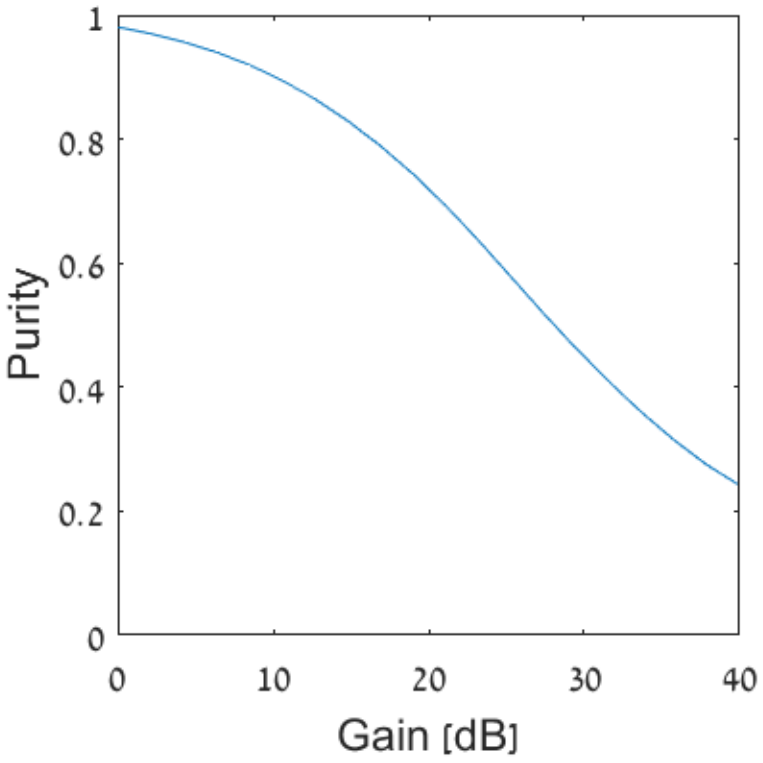

Fig. S9. Purity of the electron quantum state following a Q-PINEM interaction. The interaction is simulated with an initial photonic state from the amplifier output, ranging from coherent light state ($G = 0\ dB$) to thermal light state ($G = 40\ dB$). The average number of photons is $\langle n \rangle = 100$, the quantum coupling constant is $g_{\mathrm{q}} = 0.1$, and the initial electron energy uncertainty $\Delta E = 0.1\hbar\omega$.

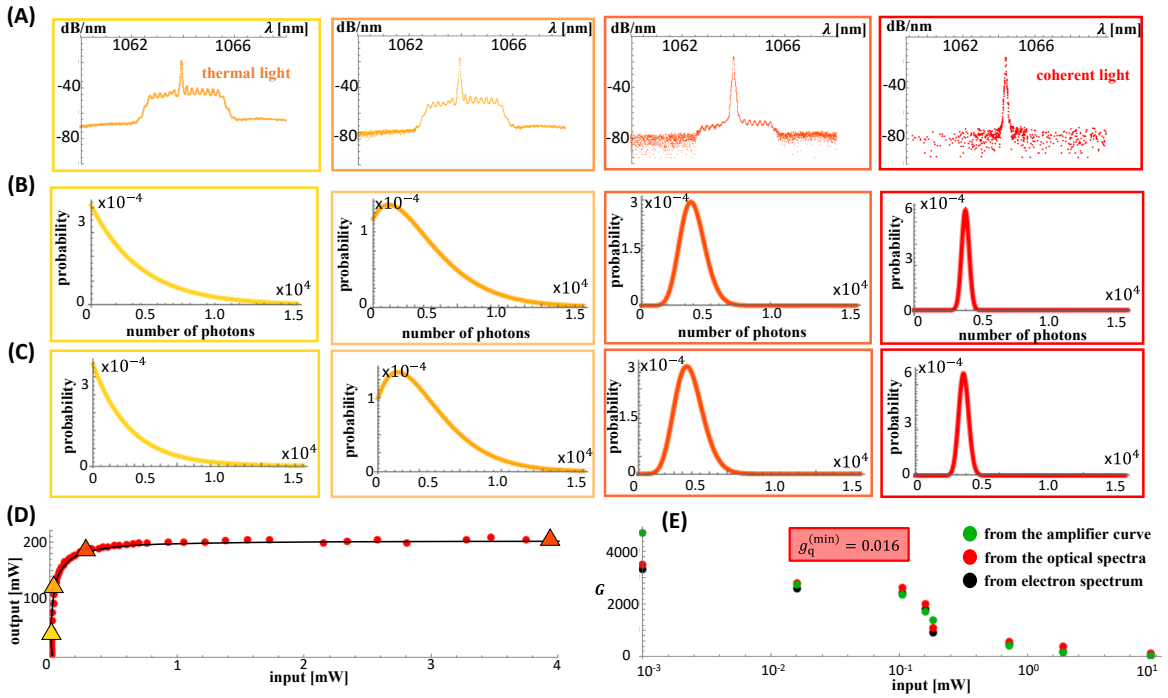

Fig. S10. Quantum optical properties of the amplifier light. We compare two methods of analysis of the quantum photon statistics of the amplifier output: **(A)** The optical spectra, from which we extract **(B)** the photon statistics. **(C)** The photon statistics can also be extracted from the measured electron energy spectra following the free-electron–light interaction. We extract the gain G of the amplifier from both experimental measurements and compare with **(D)** a direct measurement of the amplifier gain from input-output measurements. **(E)** The comparison of the three methods shows good agreement and enables us to extract the effective interaction constant g_{q} up to the coupling efficiency of light into the structure.

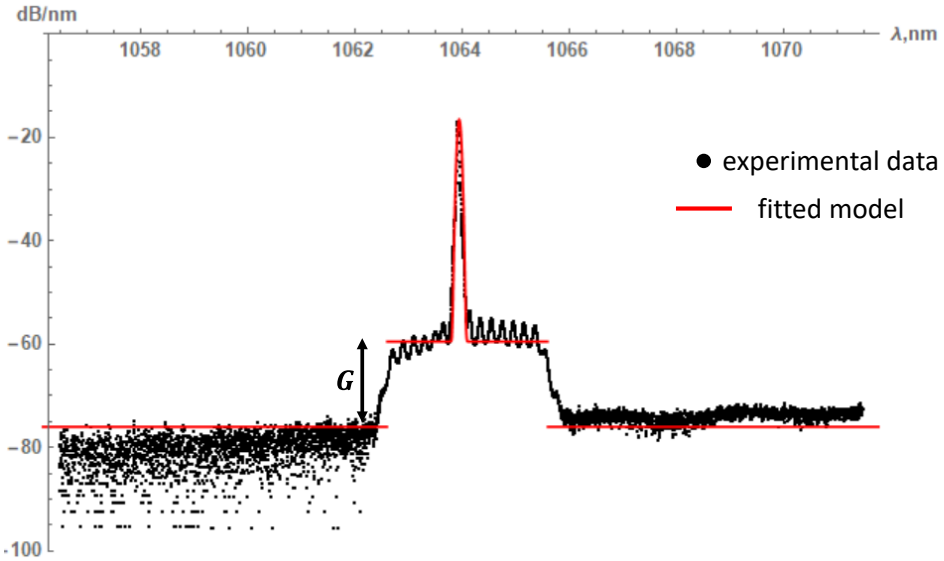

Fig. S11. Experimental optical spectrum of the amplifier output and its fit. The background noise is at -75 dB, the amplified noise is at -60 dB, and the amplified coherent input peak is at -15 dB.

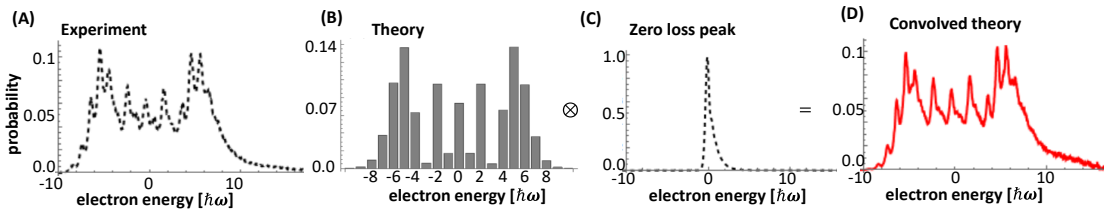

Fig. S12. Fitting theory with experiment. (A) Experimental electron energy spectrum. **(B**) The electron–light interaction theory (single-mode) according to Eq. (S4.1). **(C)** The experimental energy loss spectrum without an external light illumination. **(D)** Convolution of (B) and (C) provides a very good match with the experimental data.

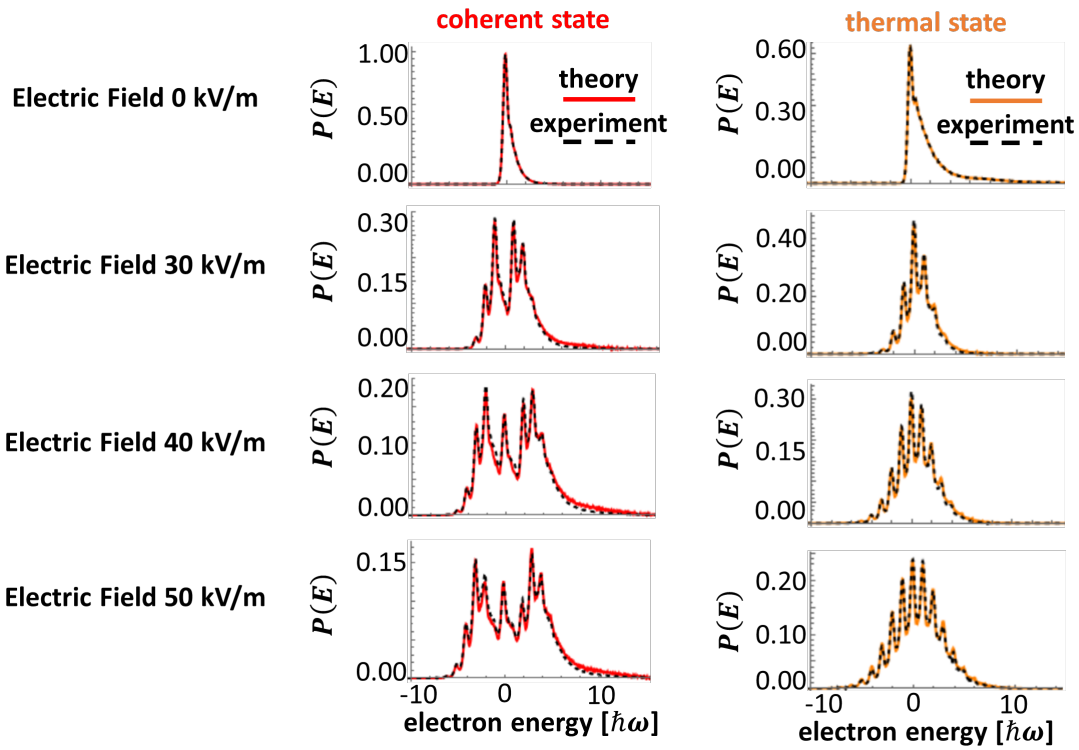

Fig. S13. Electron energy spectra for interactions with coherent and thermal states of light for selected electric field magnitudes. Colored curves show the theory, while the dashed black curves show the experimental measurements. The top panels show the electron energy spectrum without any external light illumination, i.e., the electron energy loss during its motion through the structure. The energy loss is due to spontaneous emission into various excitations as in conventional electron microscopy (combination of phonons, plasmons, Cherenkov radiation, and Smith-Purcell radiation). We use the resulting energy loss spectrum as the basic energy peak to be convolved with the discrete prediction of the Q-PINEM theory (or equivalently, the walker theory). Note that the thermal light achieves the same interaction strength as coherent state of light for the same illumination power (same field amplitude) because it maintains phase-matching in the same manner as coherent state of light. The differences in the electron energy features are due to the thermal light becoming entangled with the electron in the energy domain.

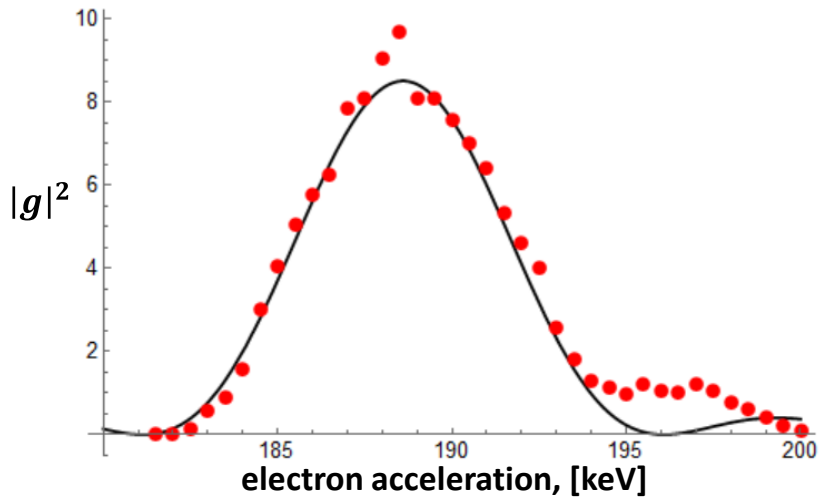

Fig. S14. Comparison between the experiment and theoretical prediction of the phase-matching condition. The figure shows the coupling strength $|g|^2$ as a function of electron acceleration, calculated according to Eq. (S5.9) (black curve) and extracted from the experiment (red dots).

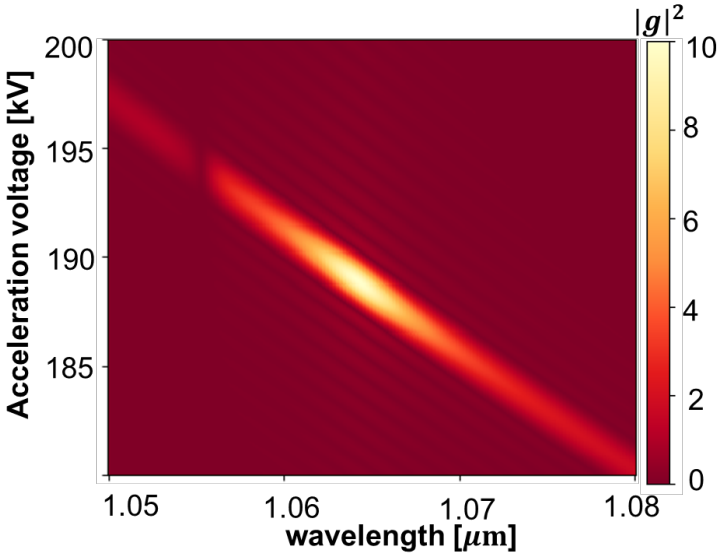

Fig. S15. Phase-matching with a longer structure. Simulation of 5-times-longer structure, 420 μm, demonstrating the concept of wavelength-selective interaction: controlling the acceleration voltage to enable probing the quantum statistics of photons at the desired frequency. This capability is especially attractive for quantum light of wide bandwidth or ultrafast pulses of quantum light.

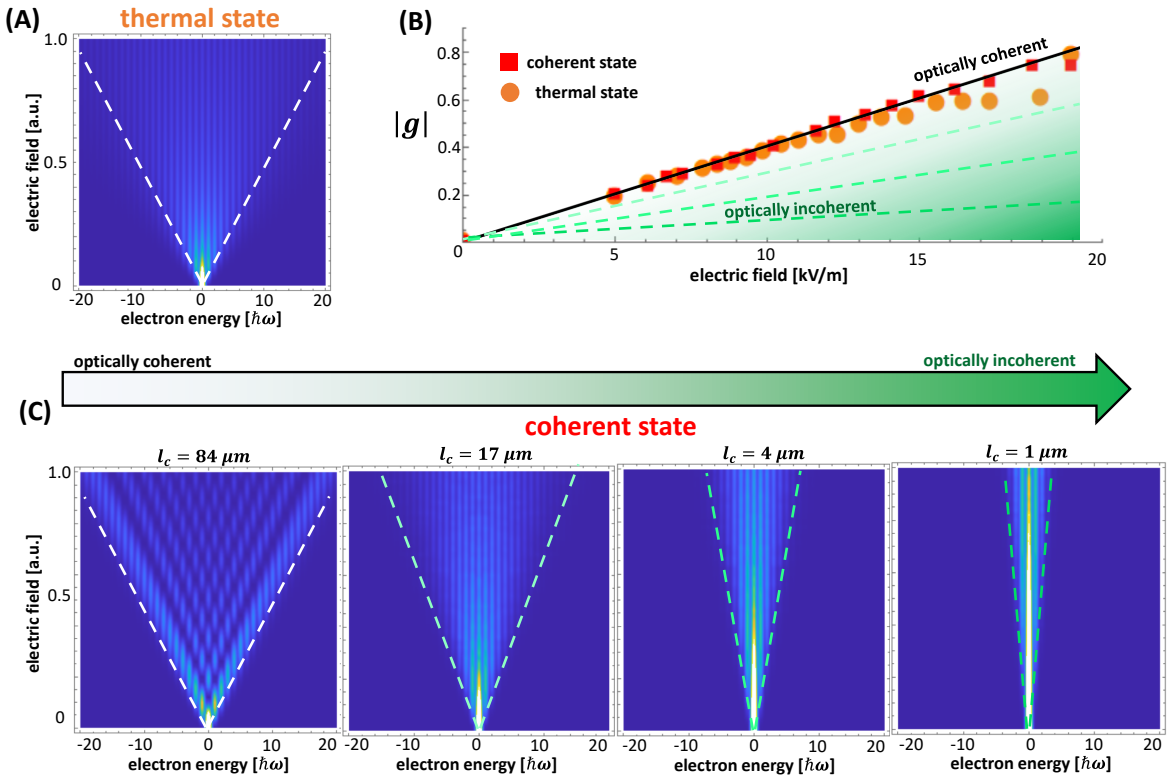

Fig. S16. The interaction of an electron with optically incoherent light. **(A)** Electron energy spectrum as a function of electric field for thermal light. **(B)** Experimental values of $|g|$ (which is proportional to the electron energy spread after the interaction) as a function of the electric field. It shows that the experimental result obtained for the thermal and coherent light states have the same slope. **(C)** Electron energy spectra as a function of electric field magnitude for coherent-state light and for different degrees of optical coherence (i.e., optical coherence lengths l_c). The energy spread decreases for shorter optical coherence lengths. The experimental results in (B) demonstrate that we have optically coherent light in both thermal and coherent interactions since the thermal and coherent light states have the same energy spread. In the simulations of this figure, the effective interaction length L is assumed to be 84 μm long.

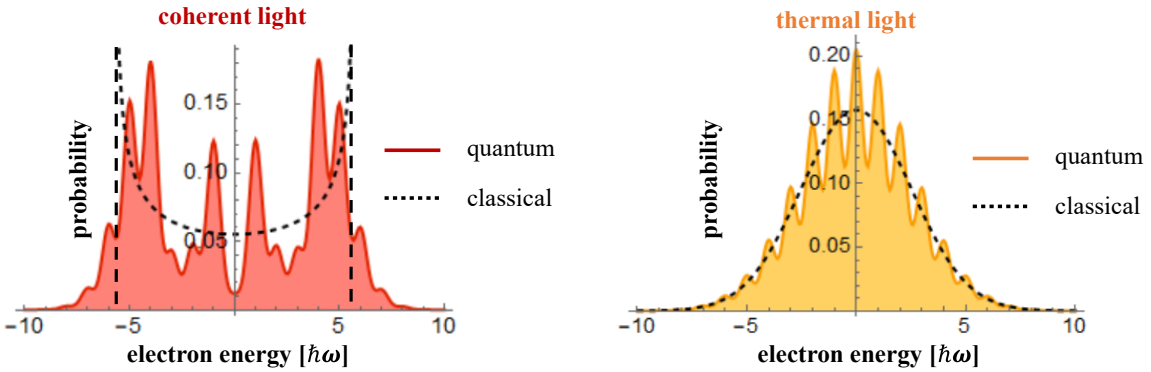

Fig. S17. Comparison between the quantum and classical theory of the PINEM and Q-PINEM interaction. The figure shows the quantum and classical descriptions of the interaction with coherent (left) state and thermal (right) state, respectively.

References and Notes

1. J. C. Maxwell, A dynamical theory of the electromagnetic field. *Philos. Trans. R. Soc. Lond.* **155**, 459–512 (1865). doi:10.1098/rstl.1865.0008

2. A. Einstein, Über einem die Erzeugung und Verwandlung des Lichtes betreffenden heuristischen Gesichtspunkt. *Ann. Phys.* **322**, 132–148 (1905). doi:10.1002/andp.19053220607

3. A. Aspect, P. Grangier, G. Roger, Experimental realization of Einstein-Podolsky-Rosen-Bohm Gedankenexperiment: A new violation of Bell's inequalities. *Phys. Rev. Lett.* **49**, 91–94 (1982). doi:10.1103/PhysRevLett.49.91

4. M. O. Scully, M. S. Zubairy, *Quantum Optics* (Cambridge Univ. Press, 1999).

5. R. Loudon, *The Quantum Theory of Light* (Oxford, 2000)

6. F. Amiranoff, S. Baton, D. Bernard, B. Cros, D. Descamps, F. Dorchies, F. Jacquet, V. Malka, J. R. Marquès, G. Matthieussent, P. Miné, A. Modena, P. Mora, J. Morillo, Z. Najmudin, Observation of laser wakefield acceleration of electrons. *Phys. Rev. Lett.* **81**, 995–998 (1998). doi:10.1103/PhysRevLett.81.995

7. T. Tajima, X. Q. Yan, T. Ebisuzaki, Wakefield acceleration. *Rev. Modern Plasma Phys.* **4**, 7 (2020). doi:10.1007/s41614-020-0043-z

8. E. A. Peralta, K. Soong, R. J. England, E. R. Colby, Z. Wu, B. Montazeri, C. McGuinness, J. McNeur, K. J. Leedle, D. Walz, E. B. Sozer, B. Cowan, B. Schwartz, G. Travish, R. L. Byer, Demonstration of electron acceleration in a laser-driven dielectric microstructure. *Nature* **503**, 91–94 (2013). doi:10.1038/nature12664 Medline

9. J. Breuer, P. Hommelhoff, Laser-based acceleration of nonrelativistic electrons at a dielectric structure. *Phys. Rev. Lett.* **111**, 134803 (2013). doi:10.1103/PhysRevLett.111.134803 Medline

10. R. J. England, R. J. Noble, K. Bane, D. H. Dowell, C.-K. Ng, J. E. Spencer, S. Tantawi, Z. Wu, R. L. Byer, E. Peralta, K. Soong, C.-M. Chang, B. Montazeri, S. J. Wolf, B. Cowan, J. Dawson, W. Gai, P. Hommelhoff, Y.-C. Huang, C. Jing, C. McGuinness, R. B. Palmer, B. Naranjo, J. Rosenzweig, G. Travish, A. Mizrahi, L. Schachter, C. Sears, G. R. Werner, R. B. Yoder, Dielectric laser accelerators. *Rev. Mod. Phys.* **86**, 1337–1389 (2014). doi:10.1103/RevModPhys.86.1337

11. N. V. Sapra, K. Y. Yang, D. Vercruysse, K. J. Leedle, D. S. Black, R. J. England, L. Su, R. Trivedi, Y. Miao, O. Solgaard, R. L. Byer, J. Vučković, On-chip integrated laser-driven particle accelerator. *Science* **367**, 79–83 (2020). doi:10.1126/science.aay5734 Medline

12. Y. Adiv *et al*. Observation of the quantum nature of laser-driven particle acceleration. CLEO conference SW4G.4. (2020).

13. B. Barwick, D. J. Flannigan, A. H. Zewail, Photon-induced near-field electron microscopy. *Nature* **462**, 902–906 (2009). doi:10.1038/nature08662 Medline

14. A. Feist, K. E. Echternkamp, J. Schauss, S. V. Yalunin, S. Schäfer, C. Ropers, Quantum coherent optical phase modulation in an ultrafast transmission electron microscope. *Nature* **521**, 200–203 (2015). doi:10.1038/nature14463 Medline

15. L. Piazza, T. T. A. Lummen, E. Quiñonez, Y. Murooka, B. W. Reed, B. Barwick, F. Carbone, Simultaneous observation of the quantization and the interference pattern of a plasmonic near-field. *Nat. Commun.* **6**, 6407 (2015). doi:10.1038/ncomms7407 Medline

16. A. Arbouet, G. M. Caruso, F. Houdellier, in *Advances in Imaging and Electron Physics*, P. W. Hawkes, Ed. (Academic Press, 2018), vol. 207, pp. 1–72.

17. F. J. García de Abajo, A. Asenjo-Garcia, M. Kociak, Multiphoton absorption and emission by interaction of swift electrons with evanescent light fields. *Nano Lett.* **10**, 1859–1863 (2010). doi:10.1021/nl100613s Medline

18. S. T. Park, M. Lin, A. H. Zewail, Photon-induced near-field electron microscopy (PINEM): Theoretical and experimental. *New J. Phys.* **12**, 123028 (2010). doi:10.1088/1367-2630/12/12/123028

19. K. E. Priebe, C. Rathje, S. V. Yalunin, T. Hohage, A. Feist, S. Schäfer, C. Ropers, Attosecond electron pulse trains and quantum state reconstruction in ultrafast transmission electron microscopy. *Nat. Photonics* **11**, 793–797 (2017). doi:10.1038/s41566-017-0045-8

20. G. M. Vanacore, I. Madan, G. Berruto, K. Wang, E. Pomarico, R. J. Lamb, D. McGrouther, I. Kaminer, B. Barwick, F. J. García de Abajo, F. Carbone, Attosecond coherent control of free-electron wave functions using semi-infinite light fields. *Nat. Commun.* **9**, 2694 (2018). doi:10.1038/s41467-018-05021-x Medline

21. Y. Morimoto, P. Baum, Diffraction and microscopy with attosecond electron pulse trains. *Nat. Phys.* **14**, 252–256 (2018). doi:10.1038/s41567-017-0007-6

22. Y. Pan, B. Zhang, A. Gover, Anomalous photon-induced near-field electron microscopy. *Phys. Rev. Lett.* **122**, 183204 (2019). doi:10.1103/PhysRevLett.122.183204 Medline

23. A. Gorlach *et al*., Ultrafast non-destructive measurement of the quantum state of light using free electrons. arXiv:2012.12069 [quant-ph] (2020).

24. C. Cohen-Tannoudji, B. Diu, F. Laloe, *Quantum Mechanics* (Wiley-Interscience, 2006), vol. 1.

25. O. Kfir, Entanglements of electrons and cavity photons in the strong-coupling regime. *Phys. Rev. Lett.* **123**, 103602 (2019). doi:10.1103/PhysRevLett.123.103602 Medline

26. V. di Giulio, M. Kociak, F. J. G. de Abajo, Probing quantum optical excitations with fast electrons. *Optica* **6**, 1524–1534 (2019). doi:10.1364/OPTICA.6.001524

27. Analogously, although unrelated to quantum walks, broader photon distributions also lead to increased decoherence in other quantum systems, such as Rabi oscillations (*86*).

28. C. A. Ryan, M. Laforest, J. C. Boileau, R. Laflamme, Experimental implementation of a discrete-time quantum random walk on an NMR quantum-information processor. *Phys. Rev. A* **72**, 062317 (2005). doi:10.1103/PhysRevA.72.062317

29. H. B. Perets, Y. Lahini, F. Pozzi, M. Sorel, R. Morandotti, Y. Silberberg, Realization of quantum walks with negligible decoherence in waveguide lattices. *Phys. Rev. Lett.* **100**, 170506 (2008). doi:10.1103/PhysRevLett.100.170506 Medline

30. M. Karski, L. Förster, J.-M. Choi, A. Steffen, W. Alt, D. Meschede, A. Widera, Quantum walk in position space with single optically trapped atoms. *Science* **325**, 174–177 (2009). doi:10.1126/science.1174436 Medline

31. F. Zähringer, G. Kirchmair, R. Gerritsma, E. Solano, R. Blatt, C. F. Roos, Realization of a quantum walk with one and two trapped ions. *Phys. Rev. Lett.* **104**, 100503 (2010). doi:10.1103/PhysRevLett.104.100503 Medline

32. P. M. Preiss, R. Ma, M. E. Tai, A. Lukin, M. Rispoli, P. Zupancic, Y. Lahini, R. Islam, M. Greiner, Strongly correlated quantum walks in optical lattices. *Science* **347**, 1229–1233 (2015). doi:10.1126/science.1260364 Medline

33. S. Dadras, A. Gresch, C. Groiseau, S. Wimberger, G. S. Summy, Quantum walk in momentum space with a Bose-Einstein condensate. *Phys. Rev. Lett.* **121**, 070402 (2018). doi:10.1103/PhysRevLett.121.070402 Medline

34. V. Kendon, Decoherence in quantum walks—A review. *Math. Structures Comput. Sci.* **17**, 1169–1220 (2007). doi:10.1017/S0960129507006354

35. M. A. Broome, A. Fedrizzi, B. P. Lanyon, I. Kassal, A. Aspuru-Guzik, A. G. White, Discrete single-photon quantum walks with tunable decoherence. *Phys. Rev. Lett.* **104**, 153602 (2010). doi:10.1103/PhysRevLett.104.153602 Medline

36. A. Schreiber, K. N. Cassemiro, V. Potoček, A. Gábris, I. Jex, Ch. Silberhorn, Decoherence and disorder in quantum walks: From ballistic spread to localization. *Phys. Rev. Lett.* **106**, 180403 (2011). doi:10.1103/PhysRevLett.106.180403 Medline

37. N. C. Harris, G. R. Steinbrecher, M. Prabhu, Y. Lahini, J. Mower, D. Bunandar, C. Chen, F. N. C. Wong, T. Baehr-Jones, M. Hochberg, S. Lloyd, D. Englund, Quantum transport simulations in a programmable nanophotonic processor. *Nat. Photonics* **11**, 447–452 (2017). doi:10.1038/nphoton.2017.95

38. K. Wang, R. Dahan, M. Shentcis, Y. Kauffmann, A. Ben Hayun, O. Reinhardt, S. Tsesses, I. Kaminer, Coherent interaction between free electrons and a photonic cavity. *Nature* **582**, 50–54 (2020). doi:10.1038/s41586-020-2321-x Medline

39. O. Kfir, H. Lourenço-Martins, G. Storeck, M. Sivis, T. R. Harvey, T. J. Kippenberg, A. Feist, C. Ropers, Controlling free electrons with optical whispering-gallery modes. *Nature* **582**, 46–49 (2020). doi:10.1038/s41586-020-2320-y Medline

40. R. Dahan, S. Nehemia, M. Shentcis, O. Reinhardt, Y. Adiv, X. Shi, O. Be'er, M. H. Lynch, Y. Kurman, K. Wang, I. Kaminer, Resonant phase-matching between a light wave and a free-electron wave function. *Nat. Phys.* **16**, 1123–1131 (2020). doi:10.1038/s41567-020-01042-w

41. M. Kozák, P. Beck, H. Deng, J. McNeur, N. Schönenberger, C. Gaida, F. Stutzki, M. Gebhardt, J. Limpert, A. Ruehl, I. Hartl, O. Solgaard, J. S. Harris, R. L. Byer, P. Hommelhoff, Acceleration of sub-relativistic electrons with an evanescent optical wave at a planar interface. *Opt. Express* **25**, 19195–19204 (2017). doi:10.1364/OE.25.019195 Medline

42. T. W. Hughes, I. A. D. Williamson, M. Minkov, S. Fan, Forward-mode differentiation of Maxwell's equations. *ACS Photonics* **6**, 3010–3016 (2019). doi:10.1021/acsphotonics.9b01238

43. G. M. Vanacore, G. Berruto, I. Madan, E. Pomarico, P. Biagioni, R. J. Lamb, D. McGrouther, O. Reinhardt, I. Kaminer, B. Barwick, H. Larocque, V. Grillo, E. Karimi, F. J. García de Abajo, F. Carbone, Ultrafast generation and control of an electron vortex beam via chiral plasmonic near fields. *Nat. Mater.* **18**, 573–579 (2019). doi:10.1038/s41563-019-0336-1 Medline

44. O. Schwartz, J. J. Axelrod, S. L. Campbell, C. Turnbaugh, R. M. Glaeser, H. Müller, Laser phase plate for transmission electron microscopy. *Nat. Methods* **16**, 1016–1020 (2019). doi:10.1038/s41592-019-0552-2 Medline

45. P. Das, J. D. Blazit, M. Tencé, L. F. Zagonel, Y. Auad, Y. H. Lee, X. Y. Ling, A. Losquin, C. Colliex, O. Stéphan, F. J. García de Abajo, M. Kociak, Stimulated electron energy loss and gain in an electron microscope without a pulsed electron gun. *Ultramicroscopy* **203**, 44–51 (2019). doi:10.1016/j.ultramic.2018.12.011 Medline

46. C. Liu, Y. Wu, Z. Hu, J. A. Busche, E. K. Beutler, N. P. Montoni, T. M. Moore, G. A. Magel, J. P. Camden, D. J. Masiello, G. Duscher, P. D. Rack, Continuous wave resonant photon stimulated electron energy-gain and electron energy-loss spectroscopy of individual plasmonic nanoparticles. *ACS Photonics* **6**, 2499–2508 (2019). doi:10.1021/acsphotonics.9b00830

47. A. Ryabov, J. W. Thurner, D. Nabben, M. V. Tsarev, P. Baum, Attosecond metrology in a continuous-beam transmission electron microscope. *Sci. Adv.* **6**, eabb1393 (2020). doi:10.1126/sciadv.abb1393 Medline

48. The coherent state $|\alpha\rangle_{\mathrm{ph}}$, electric field phasor $E_z(z)$, and time-dependent potential $\mathbf{A}(t)$ all describe the same electromagnetic field throughout the paper (*64*).

49. The nonseparable electron-photon quantum state can also involve nonlocality, once the electron and photons propagate away from the interaction area.

50. M. Shtaif, G. Eisenstein, Experimental study of the statistical properties of nonlinearly amplified signals in semiconductor optical amplifiers. *IEEE Photonics Technol. Lett.* **9**, 904–906 (1997). doi:10.1109/68.593341

51. M. Shtaif, B. Tromborg, G. Eisenstein, Noise spectra of semiconductor optical amplifiers: Relation between semiclassical and quantum descriptions. *IEEE J. Quantum Electron.* **34**, 869–878 (1998). doi:10.1109/3.668775

52. R. J. Glauber, Nobel Lecture: One hundred years of light quanta. *Rev. Mod. Phys.* **78**, 1267–1278 (2006). doi:10.1103/RevModPhys.78.1267 Medline

53. A. Reiserer, S. Ritter, G. Rempe, Nondestructive detection of an optical photon. *Science* **342**, 1349–1351 (2013). doi:10.1126/science.1246164 Medline

54. Y. Pan *et al*., Weak measurement, projective measurement and quantum-to-classical transitions in electron-photon interactions. arXiv:1910.11685 [quant-ph]. (2019)

55. R. Jozsa, Fidelity for mixed quantum states. *J. Mod. Opt.* **41**, 2315–2323 (1994). doi:10.1080/09500349414552171

56. Y. Aharonov, D. Z. Albert, L. Vaidman, How the result of a measurement of a component of the spin of a spin-1/2 particle can turn out to be 100. *Phys. Rev. Lett.* **60**, 1351–1354 (1988). doi:10.1103/PhysRevLett.60.1351 Medline

57. G. Mitchison, R. Jozsa, S. Popescu, Sequential weak measurement. *Phys. Rev. A* **76**, 062105 (2007). doi:10.1103/PhysRevA.76.062105

58. A. Feizpour, X. Xing, A. M. Steinberg, Amplifying single-photon nonlinearity using weak measurements. *Phys. Rev. Lett.* **107**, 133603 (2011). doi:10.1103/PhysRevLett.107.133603 Medline

59. M. Berry, P. Shukla, Pointer supershifts and superoscillations in weak measurements. *J. Phys. A Math. Theor.* **45**, 15301–15315 (2012). doi:10.1088/1751-8113/45/1/015301

60. B. Tamir, E. Cohen, Introduction to weak measurements and weak values. *Quanta* **2**, 7–17 (2013). doi:10.12743/quanta.v2i1.14

61. S. J. Smith, E. M. Purcell, Visible light from localized surface charges moving across a grating. *Phys. Rev.* **92**, 1069 (1953). doi:10.1103/PhysRev.92.1069

62. N. Talebi, Schrödinger electrons interacting with optical gratings: Quantum mechanical study of the inverse Smith-Purcell effect. *New J. Phys.* **18**, 123006 (2016). doi:10.1088/1367-2630/18/12/123006

63. A. Gover, Y. Pan, Dimension-dependent stimulated radiative interaction of a single electron quantum wavepacket. *Phys. Lett. A* **382**, 1550–1555 (2018). doi:10.1016/j.physleta.2018.03.049

64. Y. Pan, A. Gover, Spontaneous and stimulated emissions of a preformed quantum free-electron wave function. *Phys. Rev. A* **99**, 052107 (2019). doi:10.1103/PhysRevA.99.052107

65. V. di Giulio, F. J. García de Abajo, Free-electron shaping using quantum light. *Optica* **7**, 1820–1830 (2020). doi:10.1364/OPTICA.404598

66. A. Ben Hayun, O. Reinhardt, J. Nemirovsky, A. Karnieli, N. Rivera, I. Kaminer, Shaping quantum photonic states using free electrons. *Sci. Adv.* **7**, eabe4270 (2021). doi:10.1126/sciadv.abe4270 Medline

67. F. J. García de Abajo, V. di Giulio, Optical excitations with electron beams: Challenges and opportunities. *ACS Photonics* **8**, 945–974 (2021). doi:10.1021/acsphotonics.0c01950

68. A. Karnieli, N. Rivera, A. Arie, I. Kaminer, Superradiance and subradiance due to quantum interference of entangled free electrons. *Phys. Rev. Lett.* **127**, 060403 (2021). doi:10.1103/PhysRevLett.127.060403

69. C. Mechel, Y. Kurman, A. Karnieli, N. Rivera, A. Arie, I. Kaminer, Quantum correlations in electron microscopy. *Optica* **8**, 70 (2021). doi:10.1364/OPTICA.402693

70. O. Kfir, V. Di Giulio, F. J. G. de Abajo, C. Ropers, Optical coherence transfer mediated by free electrons. *Sci. Adv.* **7**, eabf6380 (2021). doi:10.1126/sciadv.abf6380 Medline

71. A. Karnieli, N. Rivera, A. Arie, I. Kaminer, The coherence of light is fundamentally tied to the quantum coherence of the emitting particle. *Sci. Adv.* **7**, eabf8096 (2021). doi:10.1126/sciadv.abf8096 Medline

72. R. Marchetti, C. Lacava, L. Carroll, K. Gradkowski, P. Minzioni, Coupling strategies for silicon photonics integrated chips. *Photon. Res.* **7**, 201 (2019). doi:10.1364/PRJ.7.000201

73. K. J. Leedle, A. Ceballos, H. Deng, O. Solgaard, R. F. Pease, R. L. Byer, J. S. Harris, Dielectric laser acceleration of sub-100 keV electrons with silicon dual-pillar grating structures. *Opt. Lett.* **40**, 4344–4347 (2015). doi:10.1364/OL.40.004344 Medline

74. M. Uchida, A. Tonomura, Generation of electron beams carrying orbital angular momentum. *Nature* **464**, 737–739 (2010). doi:10.1038/nature08904 Medline

75. J. Verbeeck, H. Tian, P. Schattschneider, Production and application of electron vortex beams. *Nature* **467**, 301–304 (2010). doi:10.1038/nature09366 Medline

76. B. J. McMorran, A. Agrawal, I. M. Anderson, A. A. Herzing, H. J. Lezec, J. J. McClelland, J. Unguris, Electron vortex beams with high quanta of orbital angular momentum. *Science* **331**, 192–195 (2011). doi:10.1126/science.1198804 Medline

77. N. Voloch-Bloch, Y. Lereah, Y. Lilach, A. Gover, A. Arie, Generation of electron Airy beams. *Nature* **494**, 331–335 (2013). doi:10.1038/nature11840 Medline

78. K. Y. Bliokh, I. P. Ivanov, G. Guzzinati, L. Clark, R. Van Boxem, A. Béché, R. Juchtmans, M. A. Alonso, P. Schattschneider, F. Nori, J. Verbeeck, Theory and applications of free-electron vortex states. *Phys. Rep.* **690**, 1–70 (2017). doi:10.1016/j.physrep.2017.05.006

79. R. Shiloh, R. Remez, P.-H. Lu, L. Jin, Y. Lereah, A. H. Tavabi, R. E. Dunin-Borkowski, A. Arie, Spherical aberration correction in a scanning transmission electron microscope using a sculpted thin film. *Ultramicroscopy* **189**, 46–53 (2018). doi:10.1016/j.ultramic.2018.03.016 Medline

80. O. Reinhardt, I. Kaminer, Theory of Shaping Electron Wavepackets with Light. *ACS Photonics* **7**, 2859–2870 (2020). doi:10.1021/acsphotonics.0c01133

81. G. M. Vanacore, I. Madan, F. Carbone, Spatio-temporal shaping of a free-electron wave function via coherent light–electron interaction. *Riv. Nuovo Cim.* **43**, 567–597 (2020). doi:10.1007/s40766-020-00012-5

82. A. Gover, A. Yariv, Free-electron-bound-electron resonant interaction. *Phys. Rev. Lett.* **124**, 064801 (2020). doi:10.1103/PhysRevLett.124.064801 Medline

83. S. Tsesses *et al.*, Spatial modulation of free-electron wavepackets by shaping ultrafast plasmonic excitations. CLEO *Conference* FTu3B.4 (2020).

84. M. Kozák, N. Schönenberger, P. Hommelhoff, Ponderomotive generation and detection of attosecond free-electron pulse trains. *Phys. Rev. Lett.* **120**, 103203 (2018). doi:10.1103/PhysRevLett.120.103203 Medline

85. J.-W. Henke, A. S. Raja, A. Feist, G. Huang, G. Arend, Y. Yang, J. Kappert, R. N. Wang, M. Möller, J. Pan, J. Liu, O. Kfir, C. Ropers, T. J. Kippenberg, Integrated photonics enables continuous-beam electron phase modulation. arXiv:2105.03729 [physics.optics] (2021).

86. B. W. Shore, P. L. Knight, The Jaynes-Cummings model. *J. Mod. Opt.* **40**, 1195–1238 (1993). doi:10.1080/09500349314551321

87. P. Yousefi, N. Schönenberger, J. Mcneur, M. Kozák, U. Niedermayer, P. Hommelhoff, Dielectric laser electron acceleration in a dual pillar grating with a distributed Bragg reflector. *Opt. Lett.* **44**, 1520–1523 (2019). doi:10.1364/OL.44.001520 Medline

88. T. Hughes, G. Veronis, K. P. Wootton, R. Joel England, S. Fan, Method for computationally efficient design of dielectric laser accelerator structures. *Opt. Express* **25**, 15414–15427 (2017). doi:10.1364/OE.25.015414 Medline

89. S. M. Barnett, G. Ferenczi, C. R. Gilson, F. C. Speirits, Statistics of photon-subtracted and photon-added states. *Phys. Rev. A* **98**, 013809 (2018). doi:10.1103/PhysRevA.98.013809

90. M. Selvadoray, M. S. Kumar, R. Simon, Photon distribution in two-mode squeezed coherent states with complex displacement and squeeze parameters. *Phys. Rev. A* **49**, 4957–4967 (1994). doi:10.1103/PhysRevA.49.4957 Medline

91. S. L. Braunstein, C. M. Caves, G. J. Milburn, Interpretation for a positive *P* representation. *Phys. Rev. A* **43**, 1153–1159 (1991). doi:10.1103/PhysRevA.43.1153 Medline

92. F. J. García de Abajo, Optical excitations in electron microscopy. *Rev. Mod. Phys.* **82**, 209–275 (2010). doi:10.1103/RevModPhys.82.209

93. N. Rivera, I. Kaminer, Light–matter interactions with photonic quasiparticles. *Nat. Rev. Phys.* **2**, 538–561 (2020). doi:10.1038/s42254-020-0224-2

94. M. Kozák, M. Förster, J. McNeur, N. Schönenberger, K. Leedle, H. Deng, J. S. Harris, R. L. Byer, P. Hommelhoff, Dielectric laser acceleration of sub-relativistic electrons by few-cycle laser pulses. *Nucl. Instrum. Methods Phys. Res. A* **865**, 84–86 (2017). doi:10.1016/j.nima.2016.12.051

95. A. I. Lvovsky, M. G. Raymer, M. G. Continuous-variable optical quantum-state tomography. *Rev. Mod. Phys.* **81**, 299–332 (2009). doi:10.1103/RevModPhys.81.299

96. Y. Shaked, Y. Michael, R. Z. Vered, L. Bello, M. Rosenbluh, A. Pe'er, Lifting the bandwidth limit of optical homodyne measurement with broadband parametric amplification. *Nat. Commun.* **9**, 609 (2018). doi:10.1038/s41467-018-03083-5 Medline

97. E. Knyazev, K. Y. Spasibko, M. V. Chekhova, F. Y. Khalili, Quantum tomography enhanced through parametric amplification. *New J. Phys.* **20**, 013005 (2018). doi:10.1088/1367-2630/aa99b4